Mapping *Elaeagnus umbellata* on Surface Coal Mines using Multitemporal Landsat Imagery

Adam J. Oliphant

Thesis submitted to the faculty of the Virginia Polytechnic Institute and State University in partial fulfillment of the requirements for the degree of

Master of Science
In
Forestry

Randolph H. Wynne Co-Chair
Carl E. Zipper Co-Chair
W. Mark Ford

August 6th 2015
Blacksburg, Virginia

Keywords: Afforestation, Ecosystem Recovery, Landsat, Land Cover Change, Alien Plants, Exotic Plants, Invasive Plants

Mapping *Elaeagnus umbellata* on Surface Coal Mines using Multitemporal Landsat Imagery

Adam J. Oliphant

ABSTRACT

Invasive plant species threaten native plant communities and inhibit efforts to restore disturbed landscapes. Surface coal mines in the Appalachian Mountains are some of the most disturbed landscapes in North America. Moreover, there is not a comprehensive understanding of the land cover characteristics of post- mined lands in Appalachia. Better information on mined lands' vegetative cover and ecosystem recovery status is necessary for implementation of effective environmental management practices. The invasive autumn olive (*Elaeagnus umbellata*) is abundant on former coal surface mines, often outcompeting native trees due to its faster growth rate. The frequent revisit time and spatial and spectral resolution of Landsat satellites make Landsat imagery well suited for mapping and characterizing land cover and forest recovery on former coal surface mines. I performed a multitemporal classification using a random forest analysis to map autumn olive on former and current surface coal mines in southwest Virginia. Imagery from the Operational Land Imager on Landsat 8 were used as input data for the study. Calibration and validation data for use in model development were obtained using high-resolution aerial imagery. Results indicate that autumn olive cover is sufficiently dense to enable detection using Landsat imagery on approximately 12.6% of the current and former surface coal mines located in the study area that have been mined since the early 1980s. The classified map produced here had a user's and producer's accuracy of 85.3% and 78.6% respectively for the autumn olive coverage class. Overall accuracy in reference to an independent validation dataset was 96.8%. These results indicate that autumn olive growing on reclaimed coal mines in Virginia and elsewhere in the Appalachian coalfields can be mapped using Landsat imagery. Additionally, autumn olive occurrence is a significant landscape feature on former surface coal mines in the Virginia coalfields.

DEDICATION

I dedicate my thesis to my parents, Jim Oliphant & Pat Noel who have tirelessly encouraged, pushed, and enabled me to advance to this level. I appreciate all the work, time, and money you expended to raise me. I cannot thank you enough.

ACKNOWLEDGEMENTS

I thank my great committee members for helping me along this path. I also thank my fellow remote sensing students Ranjith Gopalakrish, Ioannis Kokkinidis, Katie Britt Correll, Cameron Houser, and Jill Derwin. I would also like to thank the visiting scholars Dr. Jing Li and Qing Xia from China University of Mining and Technology for their assistance. I greatly appreciate the staff in Forest Resources and Environmental Conservation and Crop and Soil Environmental Science who assisted me. I thank Buck Kline and the Virginia Department of Forestry for helping to arrange the funding for this project. I also thank Richard Davis at the Virginia Department of Mines, Minerals, and Energy for providing coal mine permits and locations of many fields of autumn olive in Wise County. I thank the Department of Forest Recourses and Environmental Conservation for providing me with transportation and equipment. Additionally, software and computers were provided by the Center for Environmental Applications of Remote Sensing at Virginia Tech.

I thank my excellent advisors and committee member who determinedly helped me complete this thesis. I also want to thank all the great professors and staff who encouraged me along the way including: Dr. Mary Booth, Dr. Tom Jempty and Pat Blankenship at Austin Community College; Sean McKinney at Texas Commission for Environmental Quality; Dr. Ben Martin, Dr. Luyi Sun, and Dr. Richard Kimmel at Texas State University; Dr. Cully Hession, Sue Snow, and Dr. Phil Radtke at Virginia Tech.

TABLE OF CONTENTS

LIST OF FIGURES

LIST OF TABLES

LIST OF ABBREVIATIONS & DEFINITIONS

ETM+ = Enhanced Thematic Mapper Plus, an opto-mechanical, eight-band, scanning radiometer on Landsat 7, operational since 1999.

NLCD = National Land Cover Dataset, a land cover map covering the continental United States that was developed in a partnership between many Federal agencies.

NAIP = National Agriculture Imagery Program, aerial orthophotographs periodically collected by the USDA.

OLI = Operational Land Imager, a pushbroom, nine-band imaging radiometer on Landsat 8, operational since 2013.

1. INTRODUCTION

1.1 Background on Appalachian coal mining

Coal has been extracted from underground mines in the Appalachian Mountains since the 1800s (Hibbard 1990). Starting in the mid-20th century, the availability of high-capacity earth moving equipment enabled expansion of coal extraction with surface mining methods. One previously common method surface coal miners' used was "shoot and shove", where hillside rocks were fractured with dynamite to enable excavation as needed to expose coal seams. The rock above the coal seams, called overburden, was shoved off the hillside onto the slopes below to expose the coal. Mining companies often converted forested mountains into highly disturbed areas with exposed vertical rock faces and contaminated streams with high salinity, sediments, and acidity. Following decades of weak local regulation and environmental degradation, the Surface Mining and Control Reclamation Act (SMCRA) was enacted in 1977 by Congress (McElfish and Beier 1990). This law required mining operators to restore the land's approximate original contours and to re-establish vegetation after mining. Since the Act's passage, surface mining equipment has continued to increase in size, as has the extent and scale of mining disturbances in the Appalachian coalfield (Haering et al. 2004; Li et al. 2015b).

Former surface coal mines cover >600,000 hectares in the Appalachian region (Zipper et al. 2011). The SMCRA requires that mining companies return mined land to an approved land use after mining. In the 1980s and 1990s, common approved land uses were hayland pasture and wildlife habitat (US GAO 2009). Most of these lands were reclaimed using methods that caused soil surface compaction and establishment of quick-growing non-native cool season grasses and shrubs (Angel et al. 2005). Reduced soil compaction and planting of native hardwood trees has become a preferred reclamation practice since the mid-2000s (Zipper et al. 2011b). However, large areas of land reclaimed after SMCRA, using earlier reclamation practices, were reclaimed as grassland and shrubland and are not being converted to forest

through ecological succession (Zipper et al. 2011a); these landscapes are called legacy mine sites (Burger et al. 2011). Currently, researchers are investigating methods that can be applied to return legacy mines sites to native hardwood forest.

1.2 *Elaeagnus umbellata* in mine reclamation

One significant obstacle of reforestation on legacy mine sites is the invasive species *Elaeagnus umbellata*, referred to hereafter as autumn olive. Also known as Japanese silverberry or autumnberry, it is a deciduous shrub native to Japan and Northeastern Asia that can grow up to 5 m tall and 6 m wide (Black et al. 2005). Although used in North America as an ornamental shrub date for > 100 years (Parsons and Spader 1901), reports of its use on mines date from the 1960s (Sinclair 1969). It was widely planted on reclaimed mine sites in the 1980s and 1990s to provide food for wildlife, particularly birds and red foxes (*Vulpes vulpes)* and gray foxes (*Urocyon cinereoargenteus*) (Yearsley and Samuel 1980). Autumn olive was used in mine reclamation due to its tolerance of a wide range of soil conditions. Soil conditions on mine sites can be extreme, such as elevated salinity and soil pH as low as 4.0 (Smith et al. 1964).

Autumn olive is one of the few non-legumes that fixes nitrogen from the atmosphere, enabling it to grow in nutrient-poor soils such as those on former mine sites (Johnson et al. 1997). Moreover, it is able to tolerate dry soil conditions and often outcompetes native plant species in disturbed areas with full sun. It produces edible red drupes, small berries about the size of a pea, that ripen from August to October. These drupes are consumed by a wide variety of birds and other animals, enabling autumn olive seeds to be disseminated far and wide (Allan and Steiner 1972). Once autumn olive becomes established, herbicide application or repeated mechanical removal is required for eradication (Miller et al. 2010). Autumn olive can convert pasture land to a brush-inundated area in a decade (Oliphant et al. 2014).

Herbicide is often critical for controlling autumn olive. In a study that compared the effectiveness of different methods of removing established autumn olive bushes, removing

established bushes with a backhoe only stopped 15% of the bushes from re-sprouting from residual roots (Byrd et al. 2012). The most effective method of killing autumn olive was summer foliage application of imazapyr and metasulfuron methyl, where only 2% of the bushes treated re-sprouted the following year, but cost $751 per ha (Byrd et al. 2012). The most cost-effective method of controlling autumn olive was found to be a rotating fracturing brush cutter followed by hand application of herbicide to cut stumps, which cost $350 per ha treated (Byrd et al. 2012).

After assessing a completed legacy-mine reforestation project, Evans et al. (2013) reported that “Reforestation of a Wise County, Virginia, legacy mine was compromised by failure to control autumn olive effectively.” Autumn olive was present on parts of the mine site prior to reforestation. Autumn olive plants were cut prior to soil ripping, but herbicide was not applied to the plant and its roots. After soil ripping, fertilization, and planting of Appalachian native tree seedlings on the mine site, autumn olive grew rapidly from the living roots that remained in the soil. Within 4 growing seasons, much of the site were dominated by autumn olive which had overtopped the planted tree seedlings (Evans et al. 2013). Since autumn olive will outcompete hardwood saplings, understanding the spatial distribution of autumn olive is necessary for developing regional reforestation strategies (Lemke et al. 2013).

When reforesting legacy mine sites, autumn olive should be either absent or controlled otherwise it may inhibit reforestation success (Burger et al. 2011). Locating where autumn olive present or absent therefore is a prerequisite for evaluating the economic feasibility and likelihood of reforestation success on legacy mine sites. However, since the majority of former mine land is privately owned and mine sites are widely dispersed, gaining access to investigate areas on the ground for autumn olive presence and suitability for reforestation can be difficult. Therefore, development of methods for use of remote-sensing data to detect autumn olive can improve understanding of the ecosystem restoration challenges that are presented by former surface mines in the Appalachian coalfields.

1.3 Vegetation classification with remote sensing

Imagery collected from airplanes and satellites has been used for decades to describe and predict landscapes' current and potential vegetation. Often these measurements and predictions identify vegetation based on the contrast between green vegetation's strong absorbance of red light and reflectance of near infrared (NIR) light (Tucker 1979). Living green plants strongly absorb light in the red portion of the electromagnetic spectrum to synthesize molecules during photosynthesis but reflect near infrared (NIR) light since plants do not have cellular structures to use light in this region (Campbell and Wynne 2011). Multispectral remote-sensing data can aid identification of landscape features (Campbell and Wynne 2011). Applying mathematical operations to spectral-band-specific intensity values can produce vegetation indices, metrics that can be calculated from measured spectral-band values and used to identify the presence, quantity, and health of vegetation. Some pioneering works in the development and refinement of vegetation indices include the Normalized Difference Vegetation Index (NDVI) and Soil Adjusted Vegetation Index (SAVI) (Huete 1988; Rouse 1973; Tucker 1979). Further advances include the Tasselled Cap (TC) index which estimates the brightness, greenness, and wetness characteristics of an image relative to a theoretical soil line (Crist and Cicone 1984). Vegetation indices can also be used to help compensate for undesirable image artifacts caused by the look angle, solar zenith angle, and solar intensity by normalizing two or more bands from one image against one other (Campbell and Wynne 2011). This allows images of the same area, acquired on different dates, to be cross-compared so changes in vegetation due to disturbance or season can be detected. For the reasons mentioned above, vegetation indices are frequently used since they can provide information that cannot be obtained from analysis of single bands alone (Baig et al. 2014).

1.4 Landsat 8 and the Operational Land Imager

The Landsat satellite program is the longest series of earth observing satellites, extending from 1972 to the present. The Landsat imagery archive, acquired by Landsat satellites, contains a nearly continuous record of sections of the Earth's surface, which has been freely available to the public since 2008 (Roy et al. 2014). Landsat 8 was launched in February 2013. Similar to the prior Landsat satellites, it captures a nadir (straight down) image of an area every 16 days. Landsat 7 is the other satellite in the Landsat series currently in orbit. Its main sensor is the Enhanced Thematic Mapper Plus (ETM+). However, since 2003 significant portions of the ground are not imaged by the ETM+ due to the failure of the scan line corrector which results in data gaps (Markham et al. 2004).

Landsat 8 carries two sensors: the Operational Land Imager (OLI) and the Thermal Infrared Sensor (TIRS). The OLI uses a pushbroom design which allows sensors to spend more time over the ground and capture more light than sensors on earlier Landsat satellites, resulting in higher spectral accuracy and precision (Roy et al. 2014). The OLI produces images with a radiometric uncertainty of less than 3% because it was designed to be calibrated regularly by automated on-board systems that reference spectra produced by astronomical bodies including the moon, sun, and desert areas of the globe (Markham et al. 2014). Prior research found that there is a greater variability in NDVI calculated from OLI than from ETM+ in large deciduous forests and lesser variability over water bodies, indicating that the OLI has an increased ability to distinguish vegetation than prior sensors (Ke et al. 2015).

The OLI multispectral imager has nine spectral bands which capture broad sections of the electromagnetic spectrum as follows: band 1 aerosols (435 -451 nm), band 2 blue (452 -512 nm), band 3 green (533 -590 nm), band 4 red (636 -673 nm), band 5 near IR (851 -879 nm), band 6 short wave infrared (SWIR) 1 (1566 -1651 nm) and, band 7 SWIR 2 (2107 -2294 nm), band 8 panchromatic (450 -600 nm), band 9 cirrus (1300 -1350 nm). The OLI bands 1 to 7 and

9 have 30 m x 30 m ground resolution cells, hereafter referred to as pixels. Figure 1.1 shows the OLI band names and frequency ranges compared to the ETM+ imager on Landsat 7.

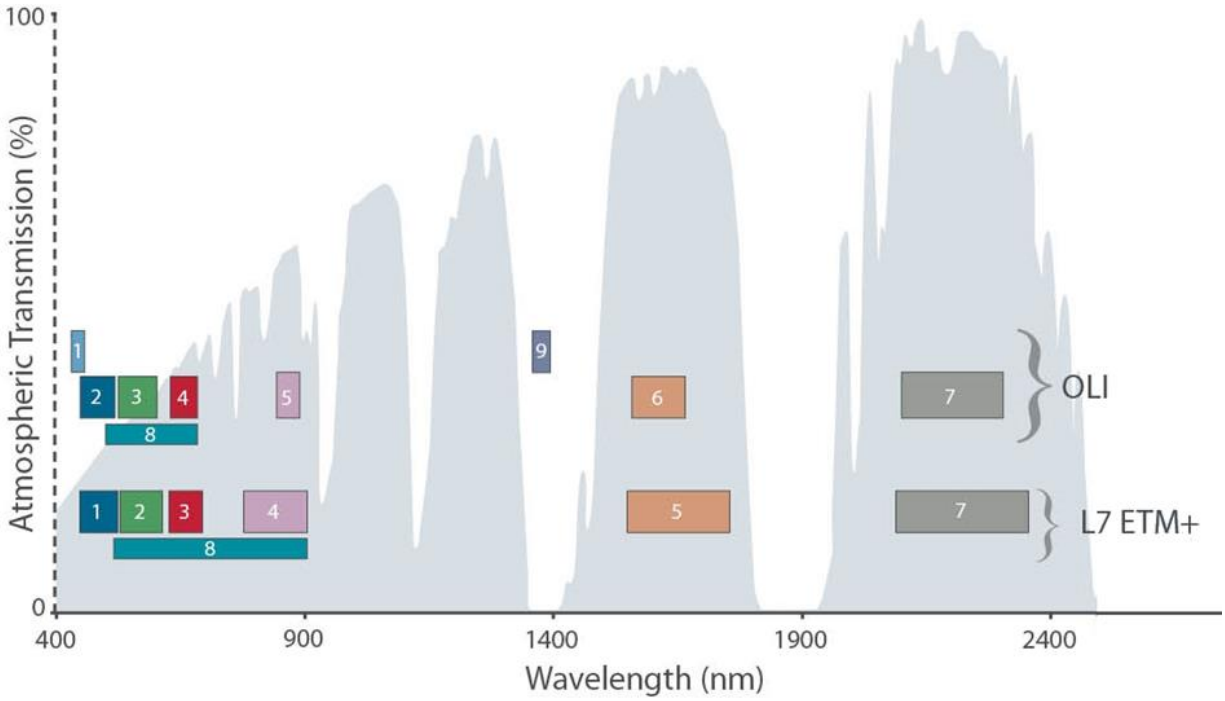

Figure 1.1 Spectral bands of the Operational Land Imager (OLI) detector flown on Landsat 8 compared to the ETM+ sensor on Landsat 7. The gray regions show the regions of the electromagnetic spectrum which are not strongly absorbed by the atmosphere. Image adapted from a figure by NASA Goddard Space Flight Center (Public domain, http://landsat.gsfc.nasa.gov/?p=3186, 2013).

Recently available Landsat 8 Surface Reflectance Climate Data Record products, distributed by United States Geological Survey (USGS), provide an additional tool for land cover classification. Surface reflectance compensates for scattering from atmospheric constituents such as aerosols, water vapor, and ozone, which are common in Appalachia. The free distribution of Landsat imagery corrected for surface reflectance product greatly reduces the preprocessing required for land classification.

1.5 Mapping plant species using phenology in remote sensing

Where most vegetation is deciduous, strong differences in reflectance and in vegetation indices are usually observed between summer and winter. Multitemporal analysis is performed when a series of images collected on different dates for an area are used to derive more information than can be acquired from an image collected on a single date. Multitemporal landcover classification has been performed using Landsat data since the mid-1970s and is becoming increasingly common thanks to widespread use of high performance computers and freely available Landsat data (Belward and de Hoyos 1987; Budreski et al. 2007; Byrne et al. 1980; Kalensky and Scherk 1975; Wulder et al. 2012). One major benefit of using multitemporal data for vegetative cover classification is the ability to detect seasonal events such as leaf out and senescence. In some instances, these phenological clues were captured by multitemporal analyses of data from multispectral sensors, which enabled species-level classifications (Table 1.1).

In the Midwestern United States, several studies have identified plant species successfully using multitemporal Landsat imagery. Twelve tree species and ten forest types were classified in northwestern Wisconsin using Landsat 5 imagery for dates determined by observations of the phenological differences among tree species (Wolter et al. 1995). In Ohio, tasseled cap (TC) wetness and brightness bands and Soil Adjusted Atmospheric Resistant Vegetation Index (SARVI2) were used to identify Amur honeysuckle (*Lonicera maackii*) (Resasco et al. 2007). Building on this work, Wilfong et al. (2009) found that NDVI for November and January proved most useful in identifying Amur honeysuckle due to spectral contrasts compared to other vegetation. In northwest Ohio, TC bands from 49 Landsat scenes were used to map invasive common and shiny buckthorn, *Frangula alnus* and *Rhamus cathartica* (Becker et al. 2013).

Multitemporal analysis of Landsat imagery has enabled changes in phenology to be observed through time. After analysis of 57 Landsat scenes extending from 1984 to 2002, Fisher et al. (2006) found that the date of leaf onset varied among years within a 13 day window in deciduous forest across New England. This study also found that urban trees leafed out 5 to 7 days before trees in unmanaged forests, and that leaf out was delayed by one day for each 4.2 meter increase in elevation. Using Moderate Resolution Imaging Spectroradiometer (MODIS) and Landsat data, Fisher and Mustard (2007) were able to predict leaf-out within 7 days of field phenology measurements at Hubbard Brook forest and Harvard forest in the northeastern United States.

When suitable phenological indicators exist, individual invasive species have been mapped with greater than 85% accuracy using Landsat data (Table 1.1). Classification was successful for species occurring in clumps greater than 0.5 ha and for species with distinctive spectral signatures (Bradley and Mustard 2006; Peterson 2005). As an example of these approaches, the invasive species glossy privet, *Ligustrum lucidum*, was successfully identified using Landsat imagery in Argentina. Because glossy privet is an evergreen species whereas the native forests are deciduous, glossy privet has a much higher NDVI than native forest species during winter months, a trait that enabled separation of glossy privet from other vegetation (Gavier-Pizarro et al. 2012; Hoyos et al. 2010). In Wolter et al. (1995), a 12 year window was required to collect 5 cloud free scenes at key dates for classifying tree species by phenological differences among tree species based on field observations. Buckthorn has a longer growing season and a slightly different phenological curve than nearby oak trees (Becker et al. 2013). However, 25 Landsat scenes over a 7 year period were used to distinguish buckthorn from surrounding oaks by using an interpolated phenological curve for each pixel (Becker et al. 2013).

Table 1.1 Species of interest, location, and accuracy statistics for selected species level classification studies conducted with multispectral Landsat imagery.

Authors	Location	Species	Type & Date of Imagery Used	Accuracy Assessment in Percent			
				Kappa	User's	Producer's	Overall
Wolter et.al. 1995	Northern Wisconsin	11 tree species	TM: June 1987 MSS: May 1992; Sept. 1985; Oct. 1980; Feb. 1988	83	96	95	84
Becker et. al. 2013	Northwest Ohio	buckthorn	TM 49 scenes, TC green	78	83	79	88
Hoyos et. al. 2010	Central Argentina	glossy privet	TM Oct. 2005; March, May, July 2006	86	97	82	89
Gavier-Pizarro et. al. 2012	Córdoba, Argentina	glossy privet	TM Dec. 1983; Feb. 1987; Jan. 1992; Nov. 1997; Jan. 2001; Mar. 2006	88	93	84	89

To distinguish vegetation types based on phenology, knowledge of when different plant species leaf-on and senesce is critical. There are databases which record phenological measurements, including the U.S. Phenological Network and Project BudBurst, which are freely accessible platforms enabling citizen scientists and professional researchers to provide and retrieve phenological data (Betancourt et al. 2005; Wolkovich and Cleland 2010). Jeong et al. (2012) mapped dates of bud break using U.S. Phenological Network data from 2009 and 2010 to create a national phenology map for potential use in tracking climate change. Species phenology has also been tracked using low cost calibrated cameras since 2008 by the PhenoCam project (Jacobs et al. 2009). However, none of these projects has data relevant to autumn olive at present.

1.6 Machine learning classifiers

Machine learning algorithms can be 'taught' to recognize patterns in data. Supervised machine learning creates predictive models from user supplied training data that can be applied to make predictions for a larger dataset, which is ideal for supervised land classification (Rodriguez-Galiano et al. 2012). Common machine learning classifiers used in remote sensing are decision trees and Support Vector Machines (SVM). Decision trees use a series of binary choices to separate data into groups called nodes. Classification and Regression Trees

(CART®) is a type of decision-tree algorithm which chooses an ideal order of variables to split data into distinct sections (Breiman et al. 1984). CART® requires smaller training data sets than several earlier techniques used in land cover classification because CART® is non parametric and resilient against extraneous variables. Earlier work found that CART® and SVM were effective in identifying autumn olive in the same study area, although the map did look very good (Oliphant et al. 2014).

RandomForests® is an ensemble of single decision trees which is useful in applications where single decision trees fail (Breiman 2001; Rodriguez-Galiano et al. 2012). The random forest algorithm is among the most frequently used and most accurate land cover classifier (Prasad et al. 2006; Rodriguez-Galiano et al. 2012). The RandomForests® classifier generates a series of decision trees from random subsets of the training data. This allows more nodes to be generated because overfitting is controlled with randomization. A portion of the reference data is randomly withheld from model training and is used for model validation (Breiman 2003). The reference data in the training and validation datasets are different for each tree which produces different decision trees. The out of bag error (OBB) is an estimate of how well the model is able to predict the validation data using the training data. Class assignments are determined by the majority of votes from all decision trees grown in the forest (Breiman 2001).

1.7 Hemispherical photography

Several studies have linked plant phenology measured on the ground to imagery acquired by satellites. The MODIS medium-resolution imagers on Terra and Aqua satellites are used to calculate vegetation productivity metrics every 8 days (Turner et al. 2006). One common metric is Leaf Area Index (LAI), the ratio of canopy leaf area to the ground area covered by the canopy. Leaf area index is defined here as one-half the total green leaf area per unit ground surface area (Chen and Cihlar 1996). True LAI measurements require physically collecting leaves by cutting down a tree or gathering leaves with buckets or mesh nets after

senescence, weighing all the leaves, and then physically measuring a sample of the leaves to develop a mass-to-area conversion. Another method involves installing a series of buckets or mesh nets that are designed to collect leaves after senescence. Since this process is very labor intensive, several LAI surrogates have been developed utilizing remote sensing instruments. Optical sensors are one surrogate, which estimates LAI by using either gap fraction or radiative transfer equations to relate leaf area to the composition of light and dark areas measured by the sensor positioned underneath canopies.

Hemispherical photos taken from a circular fish-eye lens pointed skyward can indirectly measure LAI under canopies because they record the size, shape, and distribution of gaps in tree canopies, which can then be used to describe the tree-canopy structure. Digital cameras have a high dynamic range allowing them to capture distinction between sky, leaves and branches, which is critical to calculate LAI (Jonckheere et al. 2004). Hemispherical photos are usually analyzed by specialized programs but are also visually interpretable by humans (Rich 1990). A key parameter in the software called a threshold is needed to distinguish plant matter from sky by selecting a value of light intensity that separates the two (Wagner 1998). To aid this separation, images should to be acquired during diffuse light conditions, to minimize the variation of color and intensity for sky and vegetation across the image (Jonckheere et al. 2004). The threshold value is either found through an algorithm or determined manually by choosing a value which separates sky from plant matter. Although most studies use manual interpretation, algorithms have been used to give reasonable threshold values (Nobis and Hunziker 2005; Ridler and Calvard 1978). Additionally, results are sensitive to focus and exposure and improper adjustment can cause burned out and blooming artifacts which can blur edges (Leblanc et al. 2005). Although a common use of hemispherical photography is to calculate leaf area metrics under mature tree canopies, the technique was applied recently to calculate LAI for the invasive shrubs *Ligustrum sinense* and *Lonicera maackii* (Kuebbing et al. 2014).

OBJECTIVES

My study objectives were (1) to develop a method for interpreting Landsat imagery to identify where autumn olive is a major vegetative component on former surface coal mine areas; and (2) to apply the resulting technique to identify patterns of autumn olive proliferation on former coal surface mines in the southwestern Virginia coalfield. My hypothesis is that there is a detectable spectral and phenological signal that is sufficient to separate autumn olive from other vegetation and land cover types.

2. RESEARCH METHODS

2.1 Study area

The areas of interest are lands impacted by surface coal mining in Virginia in portions of Buchannan, Dickenson, Lee, Russell, Tazewell, and Wise counties (Figure 2.1). The climate in the area is characterized by cool, wet summers and cold, snowy winters, with a mean annual temperature of 13°C, and rainfall is fairly consistent throughout the year, with a mean annual precipitation of 132 cm, (both at Big Stone Gap, Virginia) (NOAA 2015). The National Land Cover Database (NLCD) 2011 indicates that forest is the dominant land cover type in the study region. The study area is the Appalachian coalfield in Virginia (Milici et al. 2013), which is located within the Appalachian Plateaus physiographic province (Fenneman 1938), and varies in elevation above sea level from 220 to 1280 meters (Gesch et al. 2002). The area is characterized by flat-laying strata of sandstones and shales of the Mississippian and Pennsylvanian age, with interlaid coal seams (Seaber et al. 1988). Mining maps for the area were prepared by Li et al. (2015a); these maps identify surface mines by year of initial disturbance as detected by Landsat images extending from 1984 to 2011 (Li et al. 2015b).

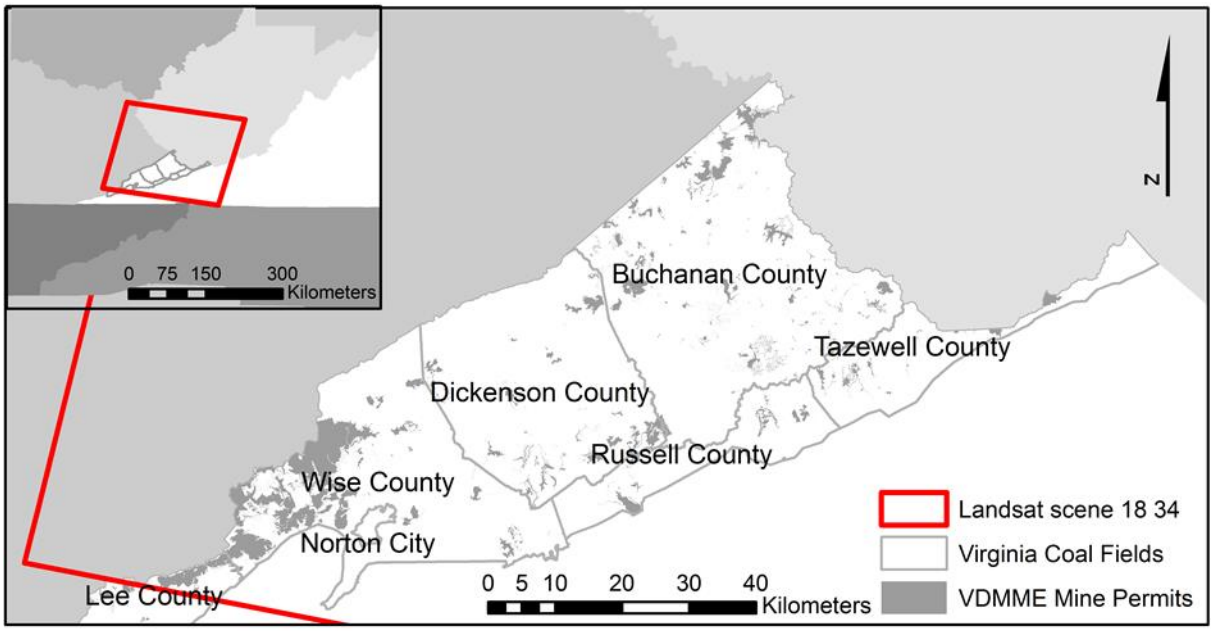

Figure 2.1 Map of study area. The red box is the extent of Landsat scene path 18 row 34. The areas in gray are current and historic surface mine permits as obtained from Virginia Department of Mines, Minerals, and Energy.

2.2 Phenological assessment

To test if autumn olive can be separated from forests using phenology at the Landsat scale, a field study was undertaken to compare the leaf coverage over time of autumn olive to a mixed hardwood forest stand. The field study was undertaken at a site near Blacksburg, Virginia, within Landsat scene path 17 row 34 in the Worldwide Reference System 2 (WRS-2). The site contained a large area of dense autumn olive that covers two OLI pixels near deciduous forest, agricultural fields, and urban areas. The two autumn olive pixels and three nearby forested pixels shared a similar aspect as recommended (Schleppi et al. 2007) so sun angle would not be a confusing factor while distinguishing classes (Figure 2.2).

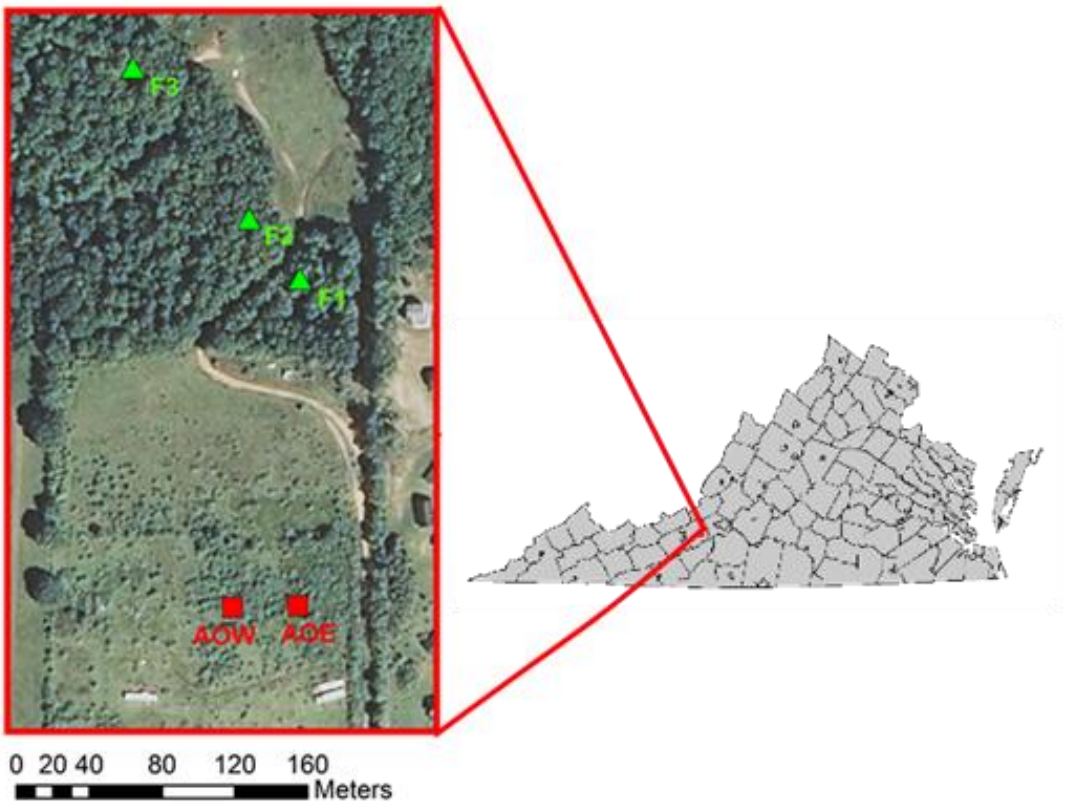

Figure 2.2 Location of field study area showing autumn olive pixels as red squares and forest pixels as green triangles. Image shows a section of the 2012 NAIP of Christiansburg Virginia.

To assess differences in phenology between mixed hardwood forest and autumn olive, LAI was calculated from images acquired by hemispherical photography at regular intervals throughout the 2014 growing season. Figure 2.3 displays a sequence of steps used to calculate LAI from acquired images. The photographs were taken using a Sigma SD10 & SD15 DSLR camera with an 8mm fisheye lens on a leveled tripod (2.3 A). LAI was calculated for three sampling points per autumn olive pixel and one sampling point in each of the three forested pixels. A stake marked each sampling point so photos could be taken in the exactly same location across the growing season.

Photos were acquired for each sampling location, most at approximately 2-week intervals, over a period extending from mid-March until November 2014. Photos were obtained by setting the camera directly over each sampling point stake to ensure images were collected

that captured the same field of view as previous images. Images were taken in diffuse light conditions during dusk or on overcast days to ensure sky conditions of uniform brightness. A 3-second shutter delay was used to eliminate vibrations caused by the technician operating the camera (Iiames et al. 2008). The camera was aligned with a compass to ensure that the top of the image was orientated towards magnetic north. Figure B.1 shows example hemispherical photos acquired for forest and autumn olive sampling areas for two different dates

The program Hemisfer 2.1 (Swiss Federal Institute for Forest, Snow, and Landscape Research 2015) was used to calculate LAI using the ellipsoidal method from the hemispherical photographs (Thimonier et al. 2010). To compensate for the non-180° field of view from the lens and camera combination, equal horizontal bars were added to the top and bottom of the images to make the native rectangular images square to simulate photos with a full 180° field of view (2.3 C). This was done so an appropriate image circle could be generated within Hemisfer (2.3 E). To better distinguish canopy from sky, the blue band was extracted since it was the band with the highest contrast (2.3 D). The simulated areas, dark areas outside the image circle, and portions of images that had persistent open sky were masked in red (2.3 D). The mask was kept consistent for the same sample point throughout the year.

An algorithm by Norbis and Hunziker (2005) was developed to separate plant matter from sky in hemispherical photos and used to set the threshold values of the images. The minimum threshold value was set at 50 and maximum at 135, the absolute minimum and maximums are 0-255 respectively (2.3 G). These values were determined by reviewing how the photos looked after the threshold was applied on photos taken during various light conditions. Parameters set in Hemisfer were 4 rings each covering a 14° arc view of sky (2.3 F). LAI was calculated from the mean of ring 3 and 4 because they are the two rings which capture the greatest amount of foliage and sky (2.3 H).

A. Hemispherical camera apparatus. The compass, 3 axis hot shoe level and tripod are shown.

B. Original image taken during an overcast day the top of the image was aligned with magnetic north.

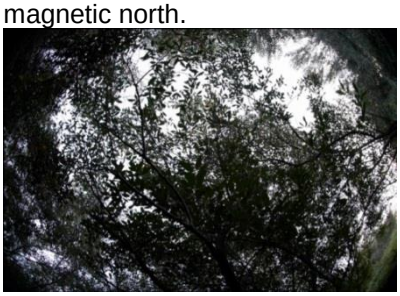

C. Solid black bars added to top and bottom of the image so an image circle could be generated.

D. Blue color band extracted from square image and red mask added to block background.

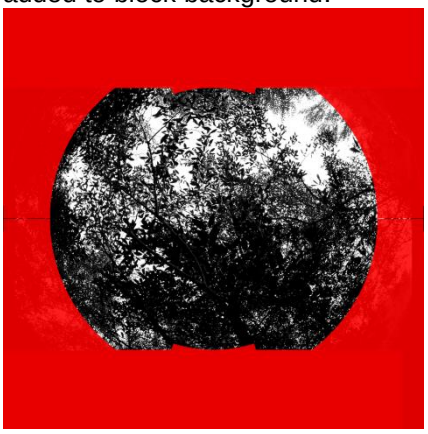

E. The black circle is the image circle. The yellow circles are the concentric image rings.

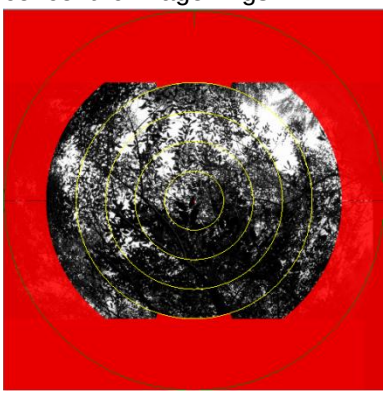

F. Image loaded into Hemisfer. Options were 4 rings, each covering a 14° arc view of sky.

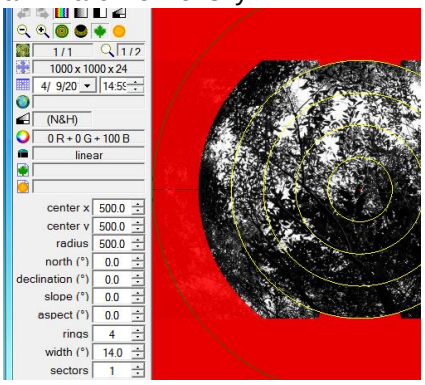

G. Threshold set by the algorithm by Nobis & Hunziker.

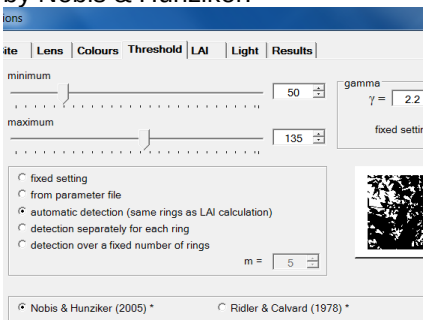

H. LAI calculated. The white and black cells are the number of sky and plant matter pixels in the image.

1	083018bmpmask.tif			
2	0.24		white	72645
3	0.0831		black	231411
4				
5	Ring 1 LAI	Ring 2 LAI	Ring 3 LAI	Ring 4 LAI
6	2.02	2.01	2.34	2.33
7	1.52	1.52	1.68	1.67
8	1.46	1.45	1.65	1.64

Figure 2.3 Steps used to calculate LAI from hemispherical photographs using Hemisfer. Images acquired by author in 2014 in Montgomery County, Virginia.

2.3 Available imagery

The majority of coal mining in Virginia has occurred in areas that are within Landsat WRS2 scene path 18, row 34 (Figure 2.1). Eight nearly cloud-free Landsat 8 scenes were downloaded from the USGS EROS Center Science Processing Architecture (ESPA) (Table 2.1) (Jenkerson 2013). Images were converted to surface reflectance by the L8SR algorithm (USGS 2015a). For ease of reference, the Landsat scenes will be referred to by acquisition date in day-of-year (for example, February 20th = 51st day-of-year). The percent cloud cover calculated by USGS was high for scenes 95, 260, and 263, but these clouds were located near the eastern edge of the scene, leaving the study area essentially cloud free. All images had a USGS Image Quality score 9 of 9.

Table 2.1 Landsat 8 imagery used in study.

Scene Identifier	Date Acquired	Day of Year	% Cloud Cover
LC80180342015010LGN00	10 January 2015	010	4.4
LC80180342014055LGN00	24 February 2014	055	2.5
LC80180342015074LGN00	15 March 2015	074	0.1
LC80180342015090LGN00	30 March 2015	090	0.1
LC80180342013095LGN01	5 April 2013	095	11.2
LC80180342013116LGN01	26 April 2013	116	0.2
LC80180342013260LGN00	17 September 2013	260	11.2
LC80180342014263LGN00	20 September 2014	263	9.3

Landsat 8 bands 1-7 corrected for surface reflectance, along with the six vegetation indices distributed by USGS (Table 2.2) were downloaded from ESPA (USGS 2015b). Most vegetation indices are calculated as band ratios which are less sensitive to topographic effects than raw spectral bands (Jin et al. 2013). NBR and NDVI are believed to be associated with some important biophysical parameters and are sensitive to forest regeneration and disturbances (Jin et al. 2013). Although primarily developed for detecting land disturbed by fire, NBR is included in other non-fire focused studies (Huang et al. 2010). Only bands and vegetation indices distributed by USGS were used in this analysis.

Table 2.2 Vegetation indices (VI) derived from Landsat 8 derived products adjusted to surface reflectance obtained from USGS EROS Science Processing Architecture. The Landsat 8 band names corresponding to the band abbreviations used here follow: B = band 3; Red = band 4; Near infrared; Infrared = band 5; Short wave infrared 1 = band 6; Short wave infrared 2 = band 7

Vegetation Index Name	Abbreviation	Equation	Reference
Normalized Difference Vegetation Index	NDVI	$\frac{B5-B4}{B5+B4}$	Rouse 1973
Enhanced Vegetation Index	EVI	$\frac{B5-B4}{B5+6*B4-0.75*B+1}$	Huete 1997
Soil-Adjusted Vegetation Index	SAVI	$1.5*\frac{B5-B4}{B5+B4+0.5B}$	Huete 1988
Modified Soil Adjusted Vegetation Index 2	MSAVI2	$\left[2*B5+1-\sqrt{(2*B5+1)^2-8(B5-B4)}\right]*\frac{1}{2}$	Qi et al. 1994
Normalized Difference Moisture Index	NDMI	$\frac{B5-B6}{B5+B6}$	Wilson and Sader 2002
Normalized Burn Ratio	NBR	$\frac{B5-B7}{B5+B7}$	Key and Benson 1999
Normalized Burn Ratio 2	NBR2	$\frac{B6-B7}{B6+B7}$	

2.4 Reference data

Training and validation data were obtained to aid model development. Due to the difficulty in accessing mine sites on the ground, acquiring training data from ground surveys was not feasible. Reference data were acquired by classifying whether autumn olive was the dominant land cover over individual Landsat pixels. Classification was done visually by cross-comparing OLI imagery with high resolution imagery from the USDA National Aerial Imagery Program (NAIP) from the years 2003 through 2014 to distinguish landcover. Edges of features such as roads, rivers, and mines were compared between the Landsat scenes and the NAIP imagery; no mis-coregistration was observed. Since it is problematic to use non-homogenous pixels for model training, pixels judged to be non-homogenous were omitted from model development.

Reference OLI pixels were chosen by randomly generating 400 plot centers within areas designated as current and past coal mining permits provided by the Virginia Department of

Mines, Minerals, and Energy (VDMME) with a minimum distance of 250 meters between plot centers. A circle with a 100 m radius was extended around each plot center and all OLI pixels within each circle were retained and classified. To demonstrate this technique, one cluster containing sample points in black was overlaid on a section of the 2014 NAIP of Wise County (Figure 2.4). Each point is the approximate center of an OLI pixel.

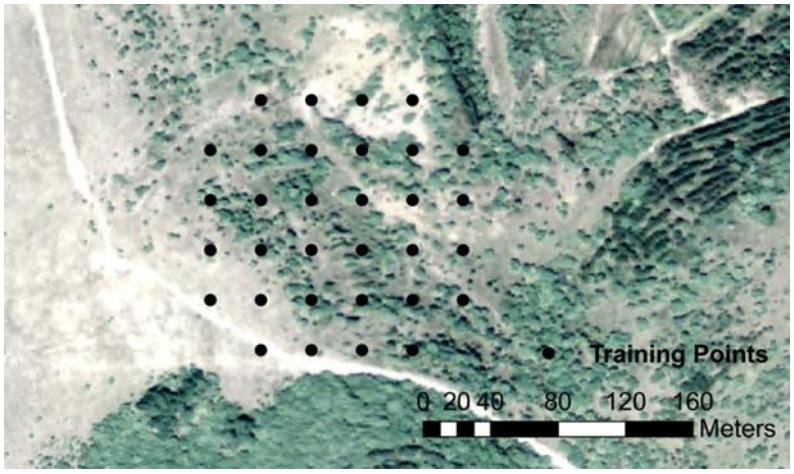

Figure 2.4 An example of a cluster used to identify training points on a section of the 2014 NAIP of Wise County, Virginia. Cluster centers were identified using a randomized procedure.

Each homogenous pixel within the 400 clusters was classified based on land cover. Homogenous pixels, as the term is used here, are those containing >85% of a single landcover type as determined visually. Eight land cover types were classified: autumn olive (dominant or co-dominant); agriculture; grass; forest; developed; active surface mines (predominantly bare ground); shrubland; and water. Other than autumn olive, these classes were easily identified visually using aerial imagery. By observing NAIP images where autumn olive was known to be present, it was found that autumn olive can be identified by these characteristics: (1) light green/gray/blue vegetation growing in or near a clearing/field; (2) apparent growth, as indicated by significant lateral expansion over 5 to 10 years; (3) forms multiple circular patches with a “popcorn” texture. Local land managers reported that autumn olive grew from seed to about 2 meters in height over roughly 10 years. They also reported that once a few scattered autumn olive bushes become established in a sunny area, many other smaller autumn olive bushes

become established in a few years and can rapidly fill the gaps between autumn olive bushes, creating a homogenous autumn olive thicket.

We decided to understand the textural characteristic of autumn olive over time. We identified several areas where autumn olive was known to be the dominant land cover. In these areas, the texture and spectral characteristics were carefully examined using NAIP and Landsat imagery. Current land cover was classified visually from 2012 and 2014 NAIP imagery. Land cover was distinguishable easily except for autumn olive which can appear similar to early successional forest. Older NAIP images from 2011, 2008, and 2003 were useful in identifying autumn olive. Autumn olive growth occurred in 5 phases (Table 2.3). A reference pixel was classified as containing autumn olive if it occurred as phase 3, 4, or 5. The shrubland class was assigned to all homogenous pixels with low apparent woody vegetation that were clearly not autumn olive. No other vegetation was observed that produced patterns resembling these phases.

Table 2.3 Five phases of autumn olive proliferation. Images acquired from 2014 NAIP images of reclaimed surface coal mines in Dickenson and Wise counties in Virginia

Proliferation Phases	Observable Characteristic	Description	Example Image
Phase 1	Location	Isolated autumn olive bushes appear on clearings, often near established forests.	
Phase 2	Growth rate	Autumn olive cover expands over following years	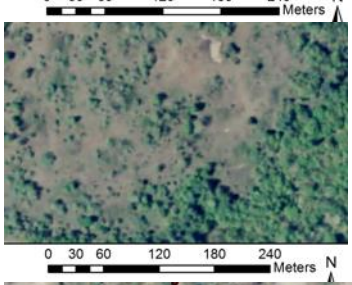
Phase 3	Reproduction	The signature of autumn olive is observed by reproduction spread from established bushes	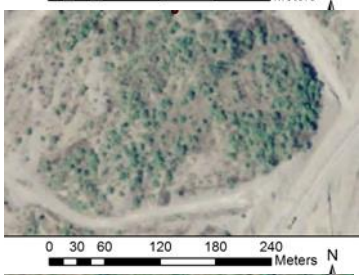
Phase 4	Growth rate	The smaller and larger autumn olive bushes continue to fill out and develop large autumn olive patches.	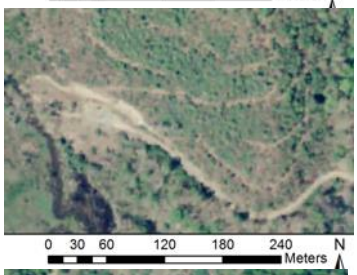
Phase 5	Texture	The gaps between the patches of autumn olive shrubs fill in and the area appears to be a blue/green mat that has an apparent texture smoother than forest but rougher than grass.	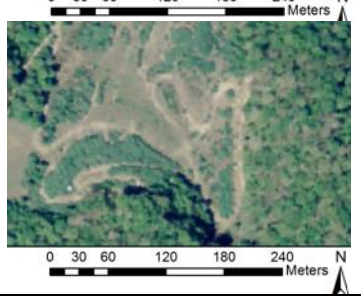

2.5 Modelling process

Although reference data were collected for six land cover classes, the visual representation of the classified map did not match the observed land cover in the NAIP imagery. There was obvious confusion between autumn olive, emerging forest, and vegetated residential areas. In order to produce the best representation of autumn olive on former surface coal mines and in accordance with research goals, the number of classes was reduced to two for classification modeling: autumn olive presence and autumn olive absence.

Classification was done with the randomForest version 4.6-10 within R 3.0.1 (Liaw and Wiener 2002; R-Core-Team 2014). Fourteen OLI bands (B) (B1, B2, B3, B4, B5, B6, B7, NDVI, EVI, SAVI, MSAVI2, MDMI, NBR, and NBR2) for each of eight Landsat scenes 10, 55, 74, 90, 95, 116, 260, and 263) were used as model predictors. The number of variables considered per node (mtry) was optimized by analyzing the effect of classification accuracy when mtry = 5, 10, 15, and 20. The default value of mtry is $\sqrt{n}$, where *n* is the number of variables. Increasing the number of trees decreased the estimated error until about 300 classification trees were created; the estimated error stabilized with additional trees. The number of trees was set to 501 since 500 is the default number of trees generated in randomForest and is commonly used in land cover classification. The reference data were randomly divided into three groups: two groups were used for model training, and one group was used for model validation. This ratio was chosen in order to have about >100 autumn olive validation points, which is twice the minimum number of validation points recommended (Congalton and Green 2008).

The reference data set was randomly divided into potential training (70%) and validation (30%) datasets. The validation dataset was unaltered, however to improve classification accuracy, the training dataset used for classification was created from pixels randomly selected from the potential training dataset. For the training dataset, the non-autumn olive pixels were subsetted from the potential training dataset (2311 to 998), for the purpose of ensuring against

over-representation of the non-autumn olive class. The autumn olive pixels were oversampled (Chen et al. 2004) by doubling them from 198 to 396. This was done to enable the randomForest model to better classify the autumn olive class. This resulted in 198 autumn olive and 2311 non-autumn olive pixels in the potential training dataset, while the actual training dataset had 396 autumn olive and 998 non-autumn olive pixels. Figure 2.5 shows the sizes of the final training and validation sets.

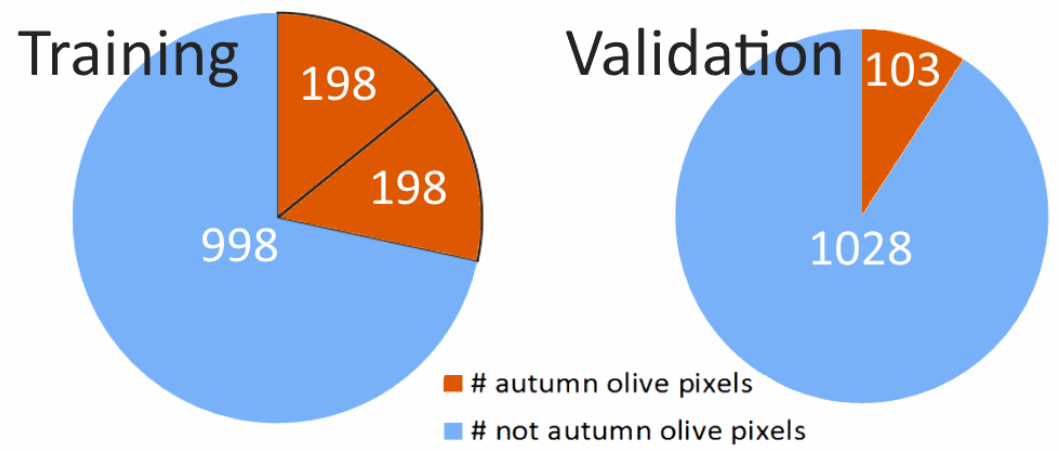

Figure 2.5 Diagram showing the distribution of the reference data into training and validation sets. The reference data was acquired on lands permitted for surface coal mining in Virginia.

An assessment of the relative importance variables had in the classification was performed for each of the 112 variables. The permutation accuracy for the out-of-bag portion of the data is recorded for every tree in the forest, and then recalculated after each predictor variable is permuted. The importance is calculated (for each variable) as the difference between the original accuracy and the accuracy obtained using the permuted variable averaged over all trees and normalized by the standard error (if it is not equal to zero). Figure 2.6 is a flow diagram that represents the modeling and accuracy assessment process.

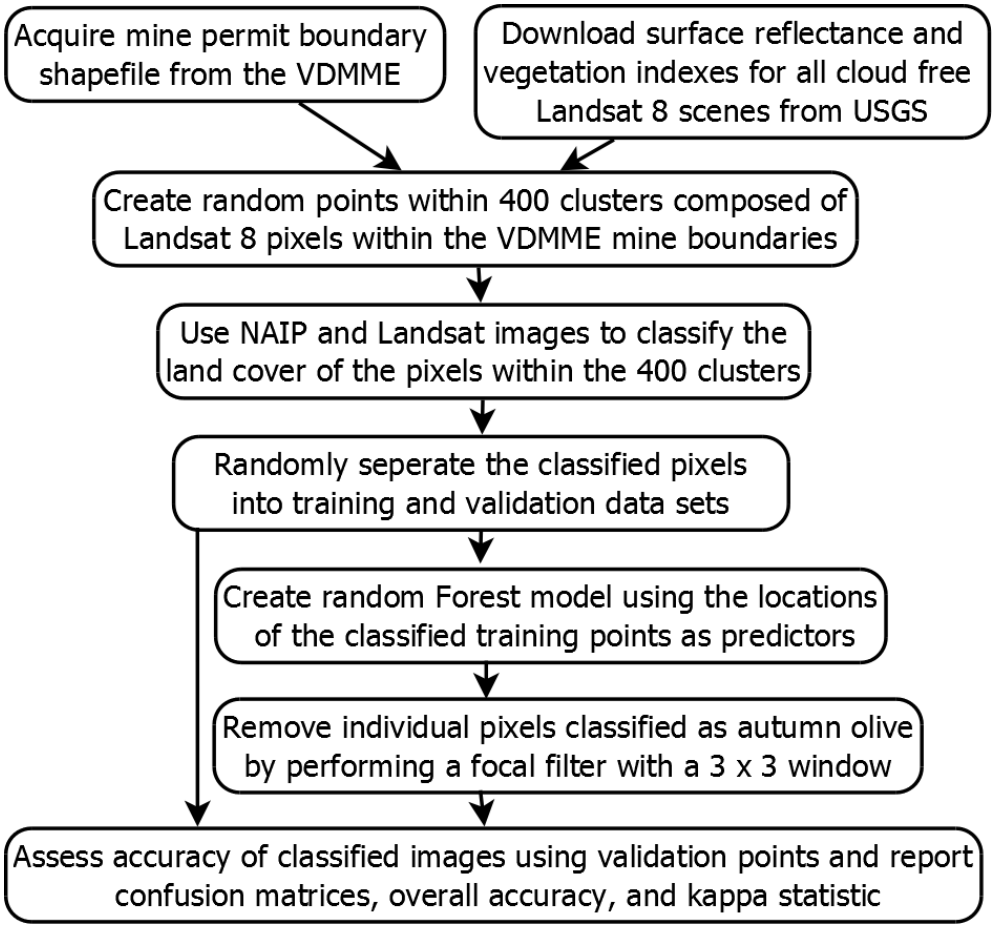

Figure 2.6 Flow diagram outlining the input data and processing steps used to generate models for presence or absence of autumn olive for the study area. VDMME = Virginia Department of Mines, Minerals, and Energy.

2.6 Determining relative importance to classification of bands and scenes

The importance of each band and scene for discriminating autumn olive was estimated by summing variable importance for all scenes and bands to show the overall effect of bands and scenes. The bands and vegetation indices for each scene were summed to show which scenes had a greater ability to distinguish autumn olive. The importance in discriminating autumn olive was summed for each band and vegetation index over all the scenes to show which bands and vegetation indices had a greater ability to distinguish autumn olive.

2.7 Post Processing

Often in pixel-based land cover classification projects, both single pixels and small numbers of pixels of one class are contained within a large homogenous area of a different class. If these isolated pixels are observed to be misclassified, they can be removed by performing a focal filter (Eliason and McEwen 1990). Focal filters are performed by comparing the class of a pixel to the classes if its neighbors. A focal window of 2 x 2 indicates that a pixel will be compared to all the pixels on its sides, while a focal window of 3 x 3 indicates that a pixel will be compared to the pixels on its sides and corners. If a pixel shares less than *n* number neighbors of the same class, the class of that pixel is changed to the class of majority of its neighbors. After several window and minimum-neighbor combinations were applied, it was decided that a 3 x 3 focal filter with a 4 pixel minimum was the best combination to remove misclassified pixels and retain correctly classified pixels based on comparison with NAIP imagery. Figure D.1 shows the percent autumn olive by county on mined land for each of the focal filters examined.

2.8 Accuracy assessment

Accuracy of classified maps was assessed based on overall accuracy in addition to user's and producer's accuracy which corresponds to commission and omission error. These metrics were assessed from an error matrix generated from a dataset which was not used to create the classified map. Figure 2.7 is an example error matrix and presents the equations used here. The rows on an error matrix correspond to the classes of areas as predicted by the resulting map, while the columns represent the actual landcover of those same areas. Overall accuracy is the number of correctly classified reference pixels divided by the total number of pixels. User's accuracy is the commission error, the probability that the reference pixels for one land cover class are correctly classified. Producer's accuracy is the omission error, the probability that all

the reference pixels are not omitted from being correctly classified. If the majority class has a high accuracy, the overall map accuracy can be quite high even if rare land classes are classified poorly. This is because each reference pixel, regardless of class, is weighted equally. Khat or ($\hat{\kappa}$) is an overall estimate of map accuracy that is robust to variations in the number reference pixels per class and allows for accuracy comparison between different classified maps (Congalton 1991). It is based on Cohen's kappa (κ) and accounts for the likelihood of pixels being classified correctly based on random chance and is given as equation (1). Because only homogenous pixels were classified, the composition of mixed pixels was not assessed, so class probabilities were estimated from pixels containing homogenous land cover classes.

	Class Z known	Class Y known	Row Total
Class Z predicted	**A** # class Z correct	**B** # incorrect	**AB** total predicted Z, A+B
Class Y predicted	**C** # incorrect	**D** # class Y correct	**CD** total predicted Y, C+D
Column Total	**AC** total known Z, A+C	**BD** total known Y, B+D	**T** grand total, A+B+C+D

Class Z User's Accuracy = $\frac{A}{A+B}$ Class Z Producer's Accuracy = $\frac{A}{A+C}$

Overall Accuracy = $\frac{A+D}{A+B+C+D}$ $\hat{\kappa} = \frac{T(A+D) - (AB*AC + CD*BD)}{T^2 - (AB*AC + CD*BD)}$

Figure 2.7 Example error matrix and equations used to assess classified map accuracy.

2.9 Determining mine land coverage

A classified map produced by Li et al. (2015a and 2015b) delineates the areas converted from dense vegetation and forest to exposed ground each year from 1984 to 2011 over the coalfields of southwest Virginia. The map is an estimate of the date mining began for areas in this region. The classified autumn olive map was overlaid on the Li et al. (2015a and 2015b) map showing the year of first mine disturbance to estimate the current percent cover of autumn olive by initial year mined. This analysis was performed for the purpose of identifying patterns of autumn olive proliferation by date of first surface mining disturbance, per Objective 2.

3. RESULTS

3.1 Phenology results

Capturing consistent photographs was difficult. Due to fading daylight, and unsuitable weather conditions, field-study photos were not collected for all sampling locations on each sampling date. Either autumn olive or forest sampling points were not collected for sampling dates 153, 182, and 278. The mean LAI for autumn olive and forest sampling across the dates sampled are shown on Figure 3.1. Numerical results of the mean forest and autumn olive LAI measurements are shown in Table B.1. Autumn olive leaves were first detected on the April 12 (day 102) images while hardwood leaves were first detected on the May 3 (day 123) images (Figure B1). Data were not collected between day 102 and 123. Figure 3.1 also shows that autumn olive had a higher LAI for days 88 through 102 but the gap between autumn olive and forested pixels was closed by day 123. An LAI gap opened up again later in the season (as detected on day 305). Both the early-season and the late-season LAI gaps, as recorded, are consistent with visual observations of the hemispherical photos.

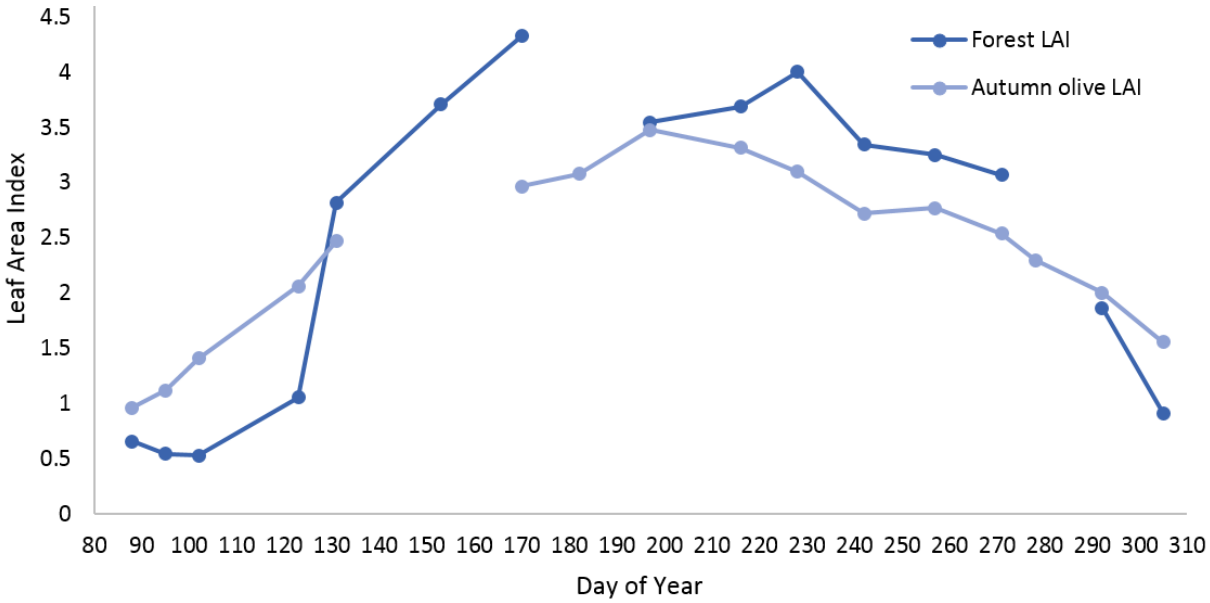

Figure 3.1 Leaf Area Index (LAI) calculated from hemispherical photos acquired at dusk at the study site in Christiansburg, Virginia in 2014. Mean LAI from rings 3 and 4 was calculated for autumn olive and mature hardwood forested pixels. The circular symbols representing measurement dates are connected by line segments.

3.2 Training classification results

By classifying the homogenous pixels within the 400 clusters, an estimate of the percent coverage of the eight landcover classes was obtained for current and former surface coal mine permits. Table 3.1 shows the count and relative abundance of the six land cover types collected for this classification.

Table 3.1 Reference data: numbers of pixels and land cover classifications.

Class	Count	% of Total
Agriculture	48	1.3
Autumn Olive	311	8.5
Developed	266	7.3
Forest	2052	56.4
Grass	300	8.2
Mine	480	13.2
Scrubland	83	2.3
Water	100	2.7
Total	3640	100.0

3.3 Map assessment

Table 3.2 shows the confusion matrix for the classified map after the 3 x 3 focal filter with a 4 pixel minimum was applied. The error matrix is populated with pixels from the independent validation data set. The out of bag estimate of error was 1.6%.

Table 3.2 Confusion matrix and accuracy assessment calculated from the independent validation dataset for the classified map after the 3 x 3 focal filter with a 4 pixel minimum was applied.

		Known			Percent Accuracy	
		AO	Other	Total	User's	Producer's
Predicted	AO	81	14	95	85.3	78.6
	Other	22	1014	1036	97.9	98.6
	Total	103	1028	1131	Overall 96.8	$\hat{\kappa}$ 0.801

I found that $\hat{\kappa}$ was resilient to inflated accuracies from a very accurately classified large class. While the overall, user's and producer's accuracy for the non-autumn olive were above 95%, the $\hat{\kappa}$ was much lower. The user's and producer's accuracy for autumn olive are on the same order as the $\hat{\kappa}$ of 0.801.

Table 3.3 shows the ten most important variables identified by randomForest. Table C.2 gives the order of importance each band scene combination had in the resulting model and in discriminating autumn olive.

Table 3.3 Ten most important variables for classifying autumn olive. The variables are labeled by DOY_band# or vegetation index. % Dec.Acc. = Percent decrease in accuracy if omitted from model

Scene & Band	Autumn olive % Dec.Acc.	Other % Dec.Acc.	Mean % Dec.Acc.	Overall Variable of Importance
116_b5	24.1	19.1	27.3	1
55_nbr2	22.5	12.9	22.8	2
116_b3	18.5	6.8	19.6	3
116_nbr2	14.9	8.5	15.5	5
74_nbr2	14.4	8.0	14.9	7
90_nbr2	14.3	9.5	14.3	9
263_b5	14.0	5.6	13.0	13
116_b6	14.0	7.8	15.2	6
116_msavi	13.8	12.3	16.1	4
260_b5	13.8	4.2	12.9	14

The summation of variables of importance by scene (Figure 3.2), and by band and vegetation index (Figure 3.3), show the relative weight each scene and band had in the randomForest classification. The Landsat scenes that proved most important to autumn olive classification were obtained on days 116 (26 April 2013), 260 (17 September 2013), and 263 (20 September 2014) (Figure 3.2). The bands that proved most important to autumn olive classification were NBR2 and B5 (Figure 3.3).

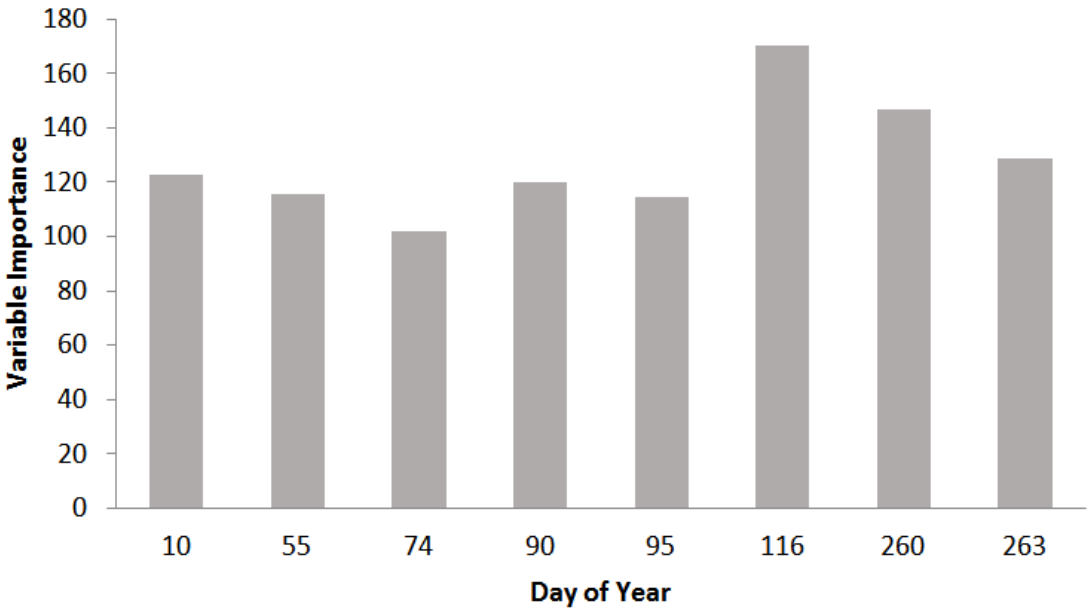

Figure 3.2 Model importance of scenes from varying phenology (denoted by the day of the year) to autumn olive classification. The importance of each scene is measured by its rank in the randomForest variable importance table. The scenes were acquired by OLI over path 18, row 34, imagery from 2013 to 2015. 10 = 10-Jan-15, 55 = 24-Feb-14, 74 = 15-Mar-15, 90 = 30-Mar-15, 95 = 5-Apr-13, 116 = 26-Apr-13, 260 = 17-Sep-13, 263 = 20-Sep-14.

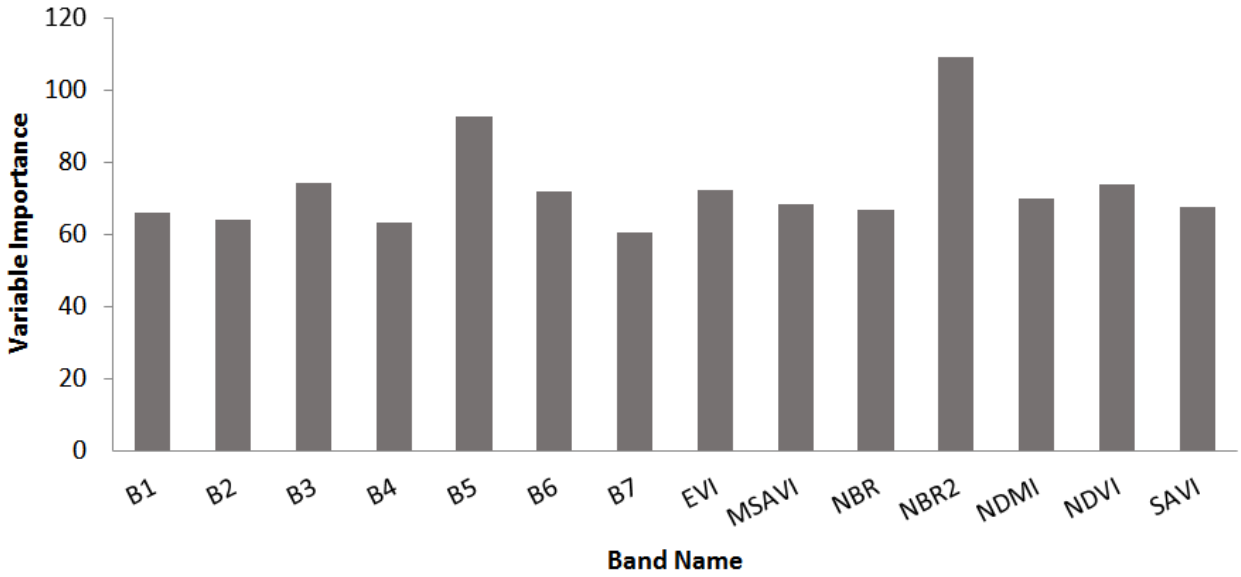

Figure 3.3 Model importance for classification of autumn olive summarized by model-input bands and vegetation indices. Bands and vegetation indices were derived from Landsat 8 path 18, row 34, imagery from 2013 to 2015.

A sample of the classified autumn olive presence-absence map overlaid on the 2014 NAIP for Wise County is shown in Figure 3.4. The area is centered on a former surface coal mine and shows various stages on reclamation and disturbance. The autumn olive classified image aligned reasonably well with existing autumn olive covered areas.

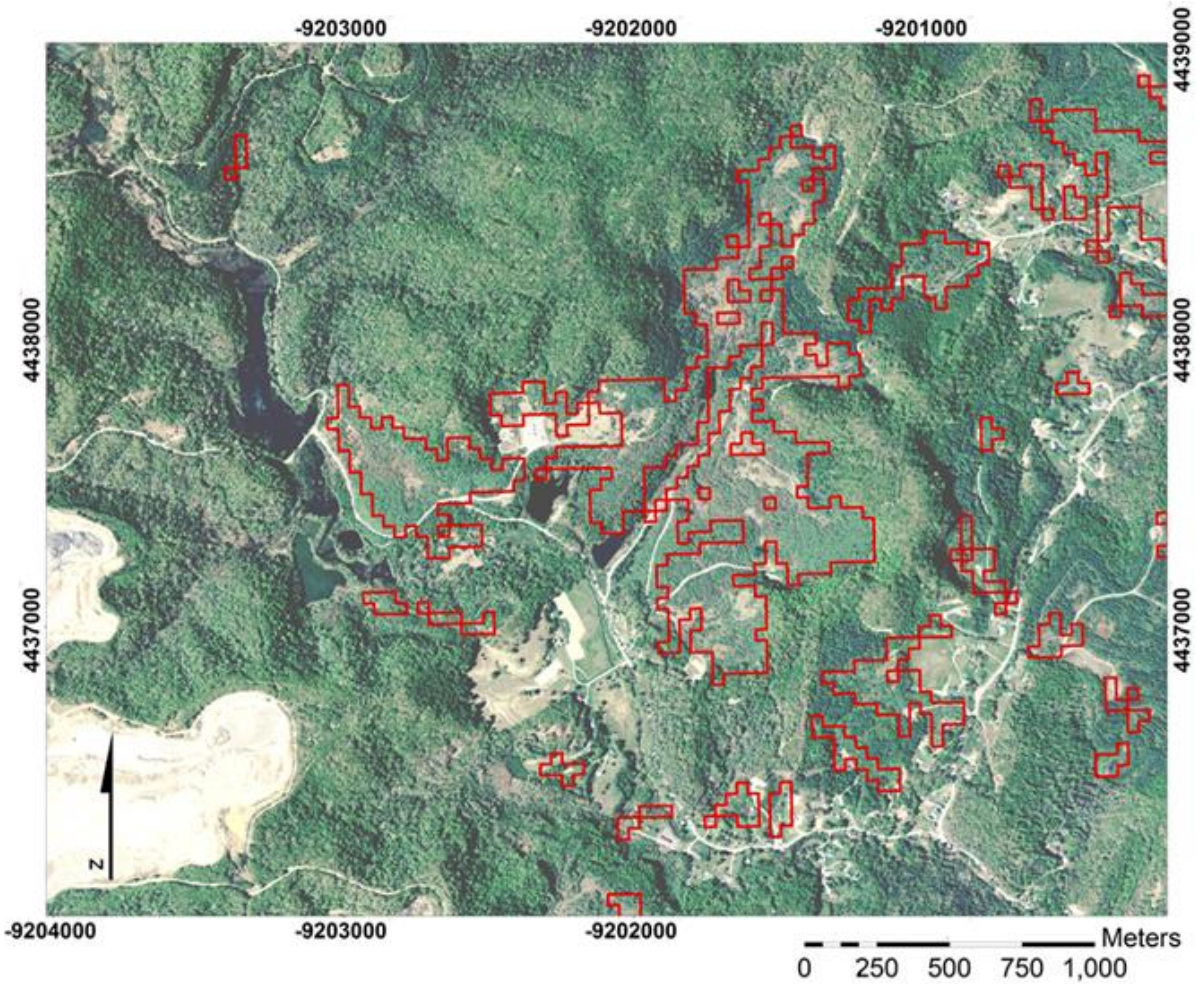

Figure 3.4 Classified areas of autumn olive from the randomForest model after the 3 x 3 focal filter with a 4 pixel minimum was applied. Autumn olive areas within red-bounded polygons are in good agreement with autumn olive on the landscape. The classified autumn olive map is overlaid on the 2014 NAIP orthoimagery acquired over Wise County, Virginia. The coordinates are in UTM 17N, WGS 1984. The bright area in the lower left-hand corner is an active surface coal mine, while the flattened area in the middle shows a reclaimed mine site.

Autumn olive was often observed on the boundaries between forest and clearings/disturbed areas. The map (Figure 3.4) supports this observation. Figure 3.5 shows the areas classified as autumn olive over 2014 NAIP imagery over the Virginia coalfields. As can be

seen by the map, areas that were classified as containing autumn olive are near bright areas which indicate active surface coal mines.

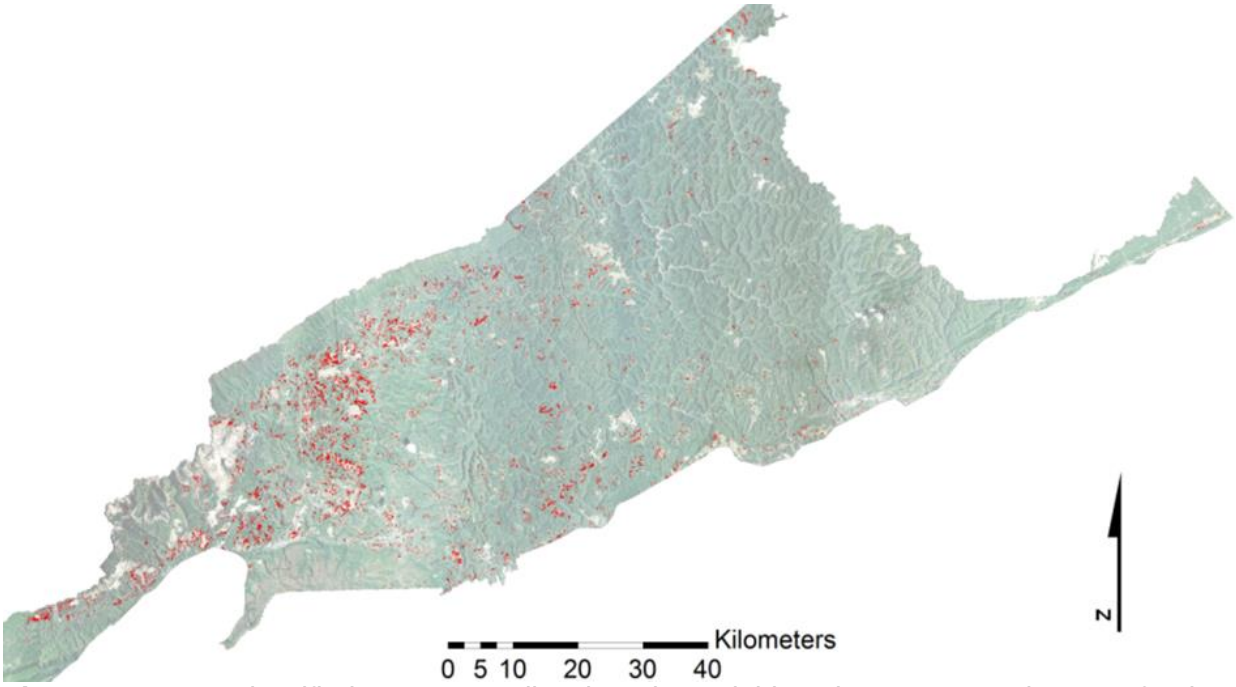

Figure 3.5 Areas classified as autumn olive, in red, overlaid on the 2014 NAIP imagery for the Virginia coalfields.

3.4 Autumn olive cover on mined areas

Of the 30,285 ha disturbed by mining in the southwestern Virginia coalfield, as detected using Landsat images extending over the 1984-2011 period (Li et al. 2015b), 3823 ha (12.6%) were classified as autumn olive cover. A total of 3605 ha of land were initially disturbed in 2001 or earlier. On those areas, 16.7% was classified as autumn-olive covered (Figure 3.6).

Figure 3.6 shows the percent autumn olive coverage on mine lands by year of initial mining-disturbance from 1984 to 2011 (Li et al. 2015a). Mining disturbance data for 1991, 1996, 2006, and 2009 are not available; however, data for the years immediately following are stated by Li et al. (2015b) as likely to include most or all of the mining disturbances occurring during the missing-data years. Table D.1 lists the areas mined by year of first detected onset, along with the autumn olive coverage expressed as both area and percent.

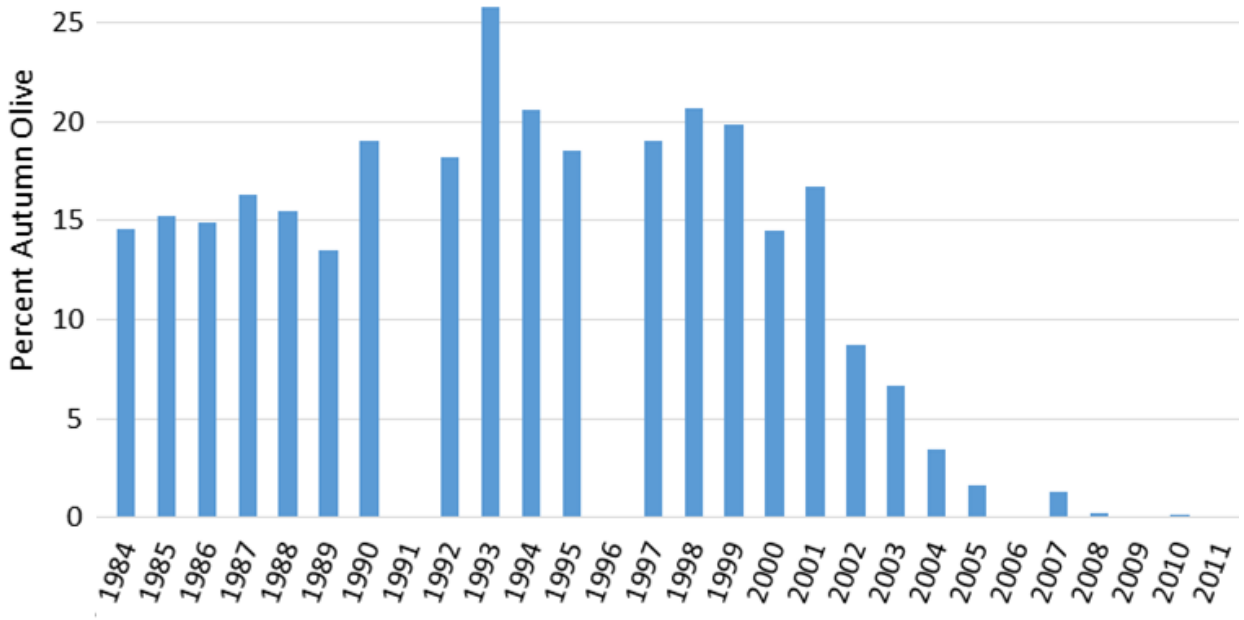

Figure 3.6 The percent autumn olive coverage (as of 2014) on coal mine areas by the date of most recent mining disturbance. Mining disturbance data for the years 1991, 1996, 2006, and 2009 are not available.

Autumn olive presently was classified as occurring on about 15% of the areas disturbed from 1984 to 1989 (Figure 3.6). For areas disturbed between 1990 and 1999, the percentage of area currently classified as autumn olive rose to about 20%. For areas disturbed between 2000 and 2007 percent classification of autumn olive ranges from 1.3% to 14.5% and increased with mine site age. For areas disturbed since 2007, autumn olive classification is less than 1% for all years. The percent coverage of autumn olive, as classified by our model, by year of first-detected mining disturbance for each county also was calculated and is shown in Table D.2.

4. DISCUSSION

4.1 Threat posed by invasive plant species

The invasive species *Elaeagnus umbellata* (autumn olive) poses a significant threat to reforestation efforts of surface coal miles in southwestern Virginia (Evans et al. 2013) and elsewhere in the central Appalachian coalfields (Zipper et al. 2011a). In order to assess this threat, this effort has generated a current landcover map of autumn olive to show where it is currently present in the coal mining region of Virginia. Statistical models based on ground data from the US Forest Service's Forest Inventory and Analysis (FIA) surveys from 2001 were used to estimate the current area covered by *Elaeagnu*s species, primarily autumn olive, to be approximately 39,000 ha in the Southeastern US (Miller et al. 2013). The coverage area is increasing at approximately 1,200 acres per year and is projected to reach around 63,400 ha by 2060 (Miller et al. 2013). Although also very common in the Piedmont of Georgia and South Carolina, autumn olive is far from being the most widespread invasive bush in the Southeastern US (Miller et al. 2013). Japanese honeysuckle is the most common invasive species in the southeastern US and is estimated to cover over 4 million ha, and may cover 5 million ha by 2060 (Miller et al. 2013). The current coverage of invasive shrubs, along with their projected future increase, highlights the need for a capability to understand and monitor distributions of invasive plants. Although invasive plant species can stabilize the soil in disturbed areas, they limit biodiversity because they exclude native species (Pyšek and Richardson 2008). Public agencies and other organizations can develop effective strategies for combatting these threats only if information such as spatial distributions and rates of spread are known. The classification method and results presented here may be of value to other efforts that seek to map invasive plant species.

4.2 Value of multitemporal analysis with Landsat imagery for species classification

This study shows that species-level classification of autumn olive patches from other land cover categories is possible with sufficient training data and imagery acquired at key times of the year. Image timing was important, because the differing phenology of autumn olive relative to surrounding native deciduous and evergreen vegetation aided separation of autumn olive dominant and co-dominant land cover from other land cover classes. Other studies have used a multitemporal approach to classify individual plant species with multispectral sensors with good success. For example, several studies have shown that species-level classifications using medium-resolution imagery had classification accuracies of > 80% (Table 1.1). In some of these cases, however, the species of interest was the only major evergreen component in an otherwise deciduous system (Gavier-Pizarro et al. 2012; Hoyos et al. 2010). In cases where this was not the case, 7 to 12 years of imagery over a given study area were required to have frequency necessary to distinguish species based on phenological patterns (Becker et al. 2013; Wolter et al. 1995).

The OLI sensor of Landsat 8 is well suited for multitemporal analysis due to its high spectral and positional accuracy. The free distribution of orthorectified and radiometrically scaled Landsat imagery since 2008 has enabled multitemporal projects to be undertaken with much greater ease than was possible before (Wulder et al. 2012). At time of writing, the USGS ESPA freely distributes higher level imagery products including top of atmosphere reflectance, surface reflectance, and vegetation indices. These products greatly reduce the preprocessing and time required for users to analyze the images before a multitemporal analysis can be performed. Also, standardized products allow results to be checked and methods to be expanded to new areas with much greater ease than if the end user had to process the imagery themselves.

A key assumption of this work is that autumn olive was correctly classified in the reference data set. It was challenging to distinguish autumn olive patches from those of other shrubs and similar low vegetation. These were used to determine the 5 phases of autumn olive proliferation shown in Table 2.3. No other land cover in the area was observed which followed these growth stages. This understanding of autumn olive growth helped in the classification of the reference data.

4.3 Visual comparisons between autumn olive classified map and NAIP imagery

Sections of the classified autumn olive map was compared to 2014 NAIP imagery to assess what spatial patterns were apparent for autumn olive growth. From this comparison, the apparent conclusion was that the majority of single pixels classified as autumn olive within large sections of mature forest were misclassifications. Hence, a 3 x 3 focal filter with a 4 pixel minimum was applied to remove the single pixels classified as autumn olive. We found that much of the autumn olive growth was at forest edges. We postulate that these edges are ideal for autumn olive establishment and growth because (1) trees enable roosting of birds, which can deposit viable seeds in their droppings, and (2) adequate sunlight is available. An observation from the reference data was the unexpectedly high amount of forest cover on mine permit areas (Table 3.1), which indicates that more than half of the areas permitted for mining were either never mined or, if mined, now have significant post-mining forest cover. Based on visual observations during classification and the mine disturbance map by year from Li et al. (2015b), it appears that the former possibility (never mined) is the more likely explanation.

4.4 Variables of importance

The relative importance of predictor variables indicates that using images with acquisition dates based on phenology is indeed useful for discriminating autumn olive from the rest of the landscape. Scene 116 (26 April 2013), scene 260 (17 September 2013), and scene 263 (20 September 2014) were the images that contributed most to discrimination of autumn

olive from other plant cover (Figure 3.3). Hence, the expectation that autumn olive's early leaf-out in spring and autumn leaf-color persistence could be used to aid autumn-olive detection was confirmed, However, other scenes also had a some ability to distinguish autumn olive, which indicates that no individual scenes or seasons fully captured the phenological and spectral characteristics that are unique to autumn olive. Scenes 90, 95 and 74 (15 March through 5 April) contributed minimally to autumn olive classification. This is likely due to the fact that autumn olive was still emerging from dormancy and had not yet produced full leaves on those dates. In prior research, a mid-November (324) Landsat scene was found to be a predictor of lower importance than scenes 116 and 263, which indicates that autumn olive leaves may have already dropped by this date (Oliphant et al. 2014). However, two studies found that November was the ideal time of year to distinguish Amur honeysuckle in Ohio (Resasco et al. 2007; Wilfong et al. 2009), indicating that the phenological characteristics that contribute to detectability differ among invasive plant species.

We found that autumn olive was distinguishable from other land covers using imagery corrected for surface reflectance. Interestingly, NBR2, which was a vegetation index created for identifying fire scars, was the strongest predictor (Figure 3.4). This indicates that magnitude differences of B7 (SWIR2) and B6 (SWIR1) are particularly useful in identifying autumn olive. The reason for this finding is not clear. The bare ground on mine sites may be spectrally similar to fire scars, but this assertion was not tested. Interestingly, B7 was the band that had the lowest contribution to the randomForest model performance. Band 5, B3, and NDVI followed NBR2 in importance; these bands are commonly used in vegetation identification. Since the identification was done with color aerial imagery, it is reasonable that band 3 (green) would be useful in identifying autumn olive. Several prior studies found that the Tasseled Cap (TC) brightness and greenness bands were useful in classifying invasive vegetation (Becker et al. 2013; Oliphant et al. 2014; Resasco et al. 2007). This study did not use TC metrics as input variables because TC coefficients are not yet available for OLI surface reflectance imagery.

4.5 Spatial and temporal patterns of autumn olive distribution

As shown in Figure 3.5 the percentage of area covered by autumn olive decreased on mine sites first disturbed from 20% in 1999 (14 to 15 years prior to the Landsat images used for our study) to 0.1% in 2011 (3 to 4 years prior to our study images). Various reasons could explain this observed pattern of current percent coverage of autumn olive versus the number of years since first disturbance. By comparing current and past aerial photographs and speaking with local experts, it is apparent that autumn olive takes about 10 years to proliferate from phase 1 to phase 4, as referenced in Table 2.3. Training areas were not classified as autumn olive unless they were at phase 3, 4, or 5. Autumn olive is no longer actively planted or used for reclamation, therefore it takes a few growing seasons for autumn olive to establish and proliferate on newly mined and reclaimed areas to become visible in aerial photos. As such, it is reasonable to conclude that autumn olive could be reliably identified and classified using aerial imagery on a site reclaimed in the range of 6 to 10 years prior to the image date.

It was found that the average Wise County surface coal mine was revegetated 6 years after initial mining disturbance by a variety of vegetation (Li et al. 2015c); however, it is not clear that this time frame is characteristic of the entire Virginia coalfield. This would suggest that autumn olive coverage may increase to the point where it becomes detectable 12 ~16 years after first disturbance, on average, although such time periods can be expected to be quite variable. This is within the year range when autumn olive increased in percent coverage as seen in Figure 3.7. Interestingly, glossy privet could not be reliably identified by Landsat imagery in Argentina until it was 10 years old; this was determined by counting tree rings in field sampling sites that were classified as containing glossy privet (Gavier-Pizarro et al. 2012).

4.6 Management and future research recommendations:

1. *Landsat imagery is adequate to map autumn olive plant cover, but further research is needed to improve mapping accuracy.*

Increasing the number of reference pixels identified by NAIP and OLI imagery would likely increase the accuracy of a future autumn olive classified map. It was challenging to classify autumn olive presence using 2012 and 2014 NAIP imagery; NAIP imagery from 2003 and 2005 has lower radiometric and spatial resolution and looked blurry and washed out compared to the most recent imagery, which hindered my ability to identify autumn olive by assessing its characteristic pattern of phased growth and proliferation (Table 2.3). With continual advances in aerial cameras, NAIP imagery continues to improve with each passing year. More detailed aerial imagery (higher spatial resolution) could aid in distinguishing autumn olive from other vegetative cover in future classification efforts.

By comparing the autumn olive classification map with 2014 NAIP imagery it is clear that the map identified the majority of emerging autumn olive patches (phases 2- 4). However, the map has a tendency to omit very dense and well established autumn patches (stage 5). This is likely because very dense autumn olive patches are spectrally similar to forest in the 260 and 263 scenes.

2. *By supplementing Landsat data with other remote-sensing data products, it is likely that mapping accuracy and detail could be improved.*

Although OLI imagery has been shown to be effective in classifying autumn olive on former and current surface coal mines in southwest Virginia, including additional data sources could increase classification accuracy. Incorporating information about vegetation height and texture from lidar data, for example, has potential to increase classification accuracy. Since lidar could distinguish mature autumn olive patches from mature forest and grassland due to their difference in height, it would increase separability between vegetation classes. As an example of such an approach, Sesnie et al. (2008) combined lidar with Landsat imagery to separate 24

vegetation cover classes over an 8000-km area in Costa Rica using a decision-tree classifier. Texture is widely used in object-based image classification using aerial data. Several species have been successfully classified using texture including the invasive Japanese knotweed (*Fallopia japonica)* (Dorigo et al. 2012).

3. *Strategic management of the autumn olive invasion will improve environmental quality and enhance ecosystem restoration potentials in central Appalachian areas that include the Virginia coalfield.*

This study found that autumn olive covers 12.6% of the lands subjected to surface mining initiated over the 1984-2011 period in southwestern Virginia. Given autumn olive's invasiveness and phased proliferation pattern (Table 2.3), the coverage of autumn olive will likely increase with time. The abundance of autumn olive bushes promotes the spread of autumn olive bushes to new areas such as recently reclaimed mine lands. Since autumn olive readily establishes on mine sites and grows faster than native vegetation, and since native forest cover often fails to develop on Appalachian surface coal mines that are not reclaimed for that purpose, autumn olive could become the dominant landcover if left unmanaged on reclaimed surface coal mines. The continued expansion of autumn olive on mined areas can be seen as a significant ecological concern. The proliferation and expansion of autumn olive on mined lands can also be seen as a concern for management of non-mined lands, given potential for autumn olive to expand from mined land areas onto adjacent lands.

4. *Improved autumn olive mapping can aid environmental management and ecosystem restoration in central Appalachian coalfield areas that include southwestern Virginia.*

Non-native shrubs, such as autumn olive, should be killed with herbicide prior to planting trees on legacy mine reforestation projects (Burger et al. 2013). If autumn olive is removed from a site, the area will no longer produce autumn-olive drupes which enable spread to new areas, such as those recently reclaimed.

5. SUMMARY AND CONCLUSIONS

This was an exploratory study to map the coverage of autumn olive over legacy mine sites in Virginia. To the author's best knowledge, no published peer-reviewed study has mapped autumn olive in Appalachia over a several county area using Landsat imagery. The classified autumn-olive map was overlaid on a recently developed map which delineates year of first Landsat-detected disturbance for surface coal mines in southwestern Virginia. Autumn olive coverage was greatest on mined lands during the 1990 – 2000 period. Results show that autumn olive presently occurs with sufficient cover to enable detection by Landsat satellites on 12.6% of the surface coal-mined lands studied. This figure is likely an underestimate of lands with autumn olive present, since the study assessed autumn olive only when present as dominant or co-dominant vegetation; lands with autumn olive present but at earlier proliferation phases were not tallied or detected. Once present on legacy mined lands, autumn olive tends to grow and proliferate. Hence, it is possible that the fraction of Virginia surface coal-mined lands occupied by autumn olive as dominant or co-dominant vegetation may increase with time.

Landsat pixels covered with autumn olive were identified using NAIP and OLI imagery and served as the reference data used to create the classified map. Multiple years of NAIP and Landsat imagery were used to increase the confidence in the landcover classification of the reference data. Since the differences between autumn olive and emerging forest can appear subtle, three factors were defined and used to classify autumn olive: landcover context, growth rate, and growth form. Only pixels identified with high confidence as autumn-olive covered were used as autumn-olive reference data.

The imagery used to detect autumn olive was restricted to the OLI sensor flown on Landsat 8. Many factors, including the frequent imagery acquisition, moderate spatial and spectral resolution, and freely available surface reflectance products, made OLI imagery uniquely suited for this study. A randomForest classifier was used to generate the classified

autumn olive map. The user's and producer's accuracies of the map were reasonably high, at 85.3% and 78.6%, respectively, and $\hat{\kappa}$ = 0.801. The most important bands and indices for distinguishing autumn olive were NBR2, NIR, green, and NDVI. OLI images acquired on 26 April 2013, 17 Sept. 2013, and 20 Sept. 2014 were the most important in distinguishing autumn olive from other land-cover classes; and a phenological comparison of autumn olive with native hardwood forest found that LAI differed for these two land cover types during those times.

Autumn olive is not only a problem on legacy mines in Virginia, as this invasive plant species is widespread across the eastern United States and Ontario, Canada (USDA NRCS 2015). Unlike hyperspectral and high spatial resolution data, Landsat imagery is regularly acquired over the entire U.S. and, at time of writing, is provided free of charge. With these two factors it may be possible to map autumn olive or other invasive plant species in other areas of the United States following techniques similar to those employed here. However, this should only be attempted if the target species has a noticeable difference in phenology than the surrounding vegetation. This work demonstrates that multitemporal Landsat 8 imagery is sufficient in classifying autumn olive on mine lands in Appalachia. Furthermore, it was found that autumn olive can be identified from human interpretation of NAIP imagery; and that autumn olive has proliferated on legacy mine sites in the Virginia coalfield.

REFERENCES

Allan PF, Steiner WW (1972) Autumn olive for wildlife and other conservation uses, June 1972 edn. U.S. Government Printing Office, Washington, D.C.

Angel P, Davis V, Burger JA, Graves D, Zipper CE (2005) The Appalachian regional reforestation initiative. U.S. Office of Surface Mining Reclamation and Enforcement, Department of Interior. Forest Reclamation Advisory No. 1.

Baig MHA, Zhang L, Shuai T, Tong Q (2014) Derivation of a tasselled cap transformation based on Landsat 8 at-satellite reflectance. Remote Sensing Letters 5:423-431

Becker RH, Zmijewski KA, Crail T (2013) Seeing the forest for the invasives: mapping buckthorn in the Oak Openings. Biological Invasions 15:315-326

Belward AS, de Hoyos A (1987) A comparison of supervised maximum likelihood and decision tree classification for crop cover estimation from multitemporal LANDSAT MSS data. International Journal of Remote Sensing 8:229-235

Betancourt JL, Schwartz MD, Breshears DD, Cayan DR, Dettinger MD, Inouye DW, Post E, Reed BC (2005) Implementing a US National Phenology Network. Eos, Transactions American Geophysical Union 86:539-539

Black BL, Fordham IM, Perkins-Veazie P (2005) Autumnberry (Elaeagnus umbellata): A Potential Cash Crop. Journal of the American Pomological Society 59:125-134

Bradley BA, Mustard JF (2006) Characterizing the Landscape Dynamics of an Invasive Plant and Risk of Invasion Using Remote Sensing. Ecological Applications 16:1132-1147

Breiman L (2001) Random forests. Machine learning 45:5-32

Breiman L (2003) Manual–Setting Up, Using and Understanding Random Forests Version 4. Dept. Statistics, University of California, Berkeley, Berkeley, CA

Breiman L, Friedman JH, Olshen RA, Stone CJ (1984) Classification and regression trees. Wadsworth, Belmont, CA

Budreski KA, Wynne RH, Browder JO, Campbell JB (2007) Comparison of segment and pixel-based non-parametric land cover classification in the Brazilian Amazon using multitemporal Landsat TM/ETM+ imagery. Photogrammetric Engineering & Remote Sensing 73:813-827

Burger JA, Zipper CE, Angel P, Eggerud S (2011) Reforestation guidelines for unused surface mined lands: Development, application, and adoption. Proceedings of American Society Mining and Reclamation, Bismarck, ND pp 11-16

Burger JA, Zipper CE, Angel PN, Hall N, Skousen JG, Barton CD, Eggerud S (2013) Establishing Native Trees on Legacy Surface Mines. U.S. Office of Surface Mining Reclamation and Enforcement, Department of Interior. Forest Reclamation Advisory No. 11.

Byrd SM, Cavender ND, Peugh CM, Bauman JM (2012) Sustainable Landscapes: Evaluating Strategies for Controlling Autumn Olive (Elaeagnus umbellata) on Reclaimed Surface Mineland at The Wilds Conservation Center in Southeastern Ohio. Journal of the American Society of Mining and Reclamation 1:1-9

Byrne GF, Crapper PF, Mayo KK (1980) Monitoring land-cover change by principal component analysis of multitemporal Landsat data. Remote Sensing of Environment 10:175-184

Campbell JB, Wynne RH (2011) Introduction to Remote Sensing. 5th edition. The Guilford Press, New York, NY

Chen C, Liaw A, Breiman L (2004) Using random forest to learn imbalanced data. Dept. Statistics, University of California, Berkeley, Berkeley, CA

Chen JM, Cihlar J (1996) Retrieving leaf area index of boreal conifer forests using Landsat TM images. Remote Sensing of Environment 55:153-162

Congalton RG (1991) A review of assessing the accuracy of classifications of remotely sensed data. Remote Sensing of Environment 37:35-46

Congalton RG, Green K (2008) Assessing the Accuracy of Remotely Sensed Data - Principles and Practices. 2nd edition. CRC Press, Boca Raton, FL

Crist EP, Cicone RC (1984) A physically-based transformation of Thematic Mapper data - The TM Tasseled Cap. IEEE Transactions on Geoscience and Remote Sensing 22:256-263

Dorigo W, Lucieer A, Podobnikar T, Carni A (2012) Mapping invasive Fallopia japonica by combined spectral, spatial, and temporal analysis of digital orthophotos. International Journal of Applied Earth Observation and Geoinformation 19:185-195

Eliason EM, McEwen AS (1990) Adaptive box filters for removal of random noise from digital images. Photogrammetric Engineering and Remote Sensing 56:453-458

Evans DM, Zipper CE, Burger JA, Strahm BD, Villamagna AM (2013) Reforestation practice for enhancement of ecosystem services on a compacted surface mine: Path toward ecosystem recovery. Ecological Engineering 51:16-23

Fenneman NM (1938) Physiography of Eastern United States. McGraw Hill, New York, NY

Fisher JI, Mustard JF (2007) Cross-scalar satellite phenology from ground, Landsat, and MODIS data. Remote Sensing of Environment 109:261-273

Gavier-Pizarro GI, Kuemmerle T, Hoyos LE, Stewart SI, Huebner CD, Keuler NS, Radeloff VC (2012) Monitoring the invasion of an exotic tree (Ligustrum lucidum) from 1983 to 2006 with Landsat TM/ETM+ satellite data and Support Vector Machines in Córdoba, Argentina. Remote Sensing of Environment 122:134-145

Gesch D, Oimoen M, Greenlee S, Nelson C, Steuck M, Tyler D (2002) The national elevation dataset. Photogrammetric Engineering and Remote Sensing 68:5-32

Haering KC, Daniels WL, Galbraith JM (2004) Appalachian mine soil morphology and properties. Soil Science Society of America Journal 68:1315-1325

Hibbard WR (1990) Virginia Coal: An Abridged History and Complete Data Manual of Virginia Coal Production/consumption from 1748 to 1988. Virginia Center for Coal and Energy Research. Virginia Tech, Blacksburg, VA

Hoyos LE, Gavier-Pizarro GI, Kuemmerle T, Bucher EH, Radeloff VC, Tecco PA (2010) Invasion of glossy privet (Ligustrum lucidum) and native forest loss in the Sierras Chicas of Córdoba, Argentina. Biological Invasions 12:3261-3275

Huang C, Goward SN, Masek JG, Thomas N, Zhu Z, Vogelmann JE (2010) An automated approach for reconstructing recent forest disturbance history using dense Landsat time series stacks. Remote Sensing of Environment 114:183-198

Huete AR (1988) A soil-adjusted vegetation index (SAVI). Remote Sensing of Environment 25:295-309

Huete AR, Liu H, Van Leeuwen WJ (1997) The use of vegetation indices in forested regions: issues of linearity and saturation. In: Proceedings of IGARSS ’97—

International Geoscience and Remote Sensing Seminar. ESA Publications, Noordwijk, pp 1966–1968

Iiames JS, Congalton RG, Pilant AN, Lewis TE (2008) Leaf area index (LAI) change detection analysis on Loblolly pine (Pinus taeda) following complete understory removal. Photogrammetric Engineering & Remote Sensing 74:1389-1400

Jacobs N, Burgin W, Fridrich N, Abrams A, Miskell K, Braswell BH, Richardson AD, Pless R (2009) The global network of outdoor webcams: properties and applications. In: Proceedings of the 17th ACM SIGSPATIAL International Conference on Advances in Geographic Information Systems, Seattle, WA pp 111-120

Jenkerson C (2013) User guide: Earth resources observation and science (EROS) center science processing architecture (ESPA) on demand interface. U.S. Geological Survey Edition 1.4

Jin S, Yang L, Danielson P, Homer C, Fry J, Xian G (2013) A comprehensive change detection method for updating the National Land Cover Database to circa 2011. Remote Sensing of Environment 132:159-175

Johnson GV, Schwintzer CR, Tjepkema JD (1997) The acetylene-induced decline in nitrogenase activity in root nodules of Elaeagnus angustifolia. Plant and Soil 191:157-161

Jonckheere I, Fleck S, Nackaerts K, Muys B, Coppin P, Weiss M, Baret F (2004) Review of methods for in situ leaf area index determination: Part I. Theories, sensors and hemispherical photography. Agricultural and forest meteorology 121:19-35

Kalensky Z, Scherk LR Accuracy of forest mapping from Landsat computer compatible tapes. (1975) In: Proceedings of the 10th International Symposium on Remote Sensing of Environment, Ann Arbor, MI pp 1159-1167

Ke Y, Im J, Lee J, Gong H, Ryu Y (2015) Characteristics of Landsat 8 OLI-derived NDVI by comparison with multiple satellite sensors and in-situ observations. Remote Sensing of Environment 164:298–313

Key CH, Benson NC (1999) Measuring and remote sensing of burn severity. In Proceedings Joint Fire Science Conference and Workshop, vol. II, Moscow, ID pp 284

Kuebbing SE, Classen AT, Simberloff D (2014) Two co-occurring invasive woody shrubs alter soil properties and promote subdominant invasive species. Journal of Applied Ecology 51:124-133

Leblanc SG, Chen JM, Fernandes R, Deering DW, Conley A (2005) Methodology comparison for canopy structure parameters extraction from digital hemispherical photography in boreal forests. Agricultural and Forest Meteorology 129:187-207

Lemke D, Schweitzer CJ, Tadesse W, Wang Y, Brown JA (2013) Geospatial Assessment of Invasive Plants on Reclaimed Mines in Alabama. Invasive Plant Science and Management 6:401-410

Li J, Donovan PF, Zipper CE, Wynne RH, Oliphant AJ (2015a) Mining disturbances in Virginia's southwestern coalfield, 1984-2011.doi:http://dx.doi.org/10.7294/W47P8W97

Li J, Zipper CE, Donovan PF, Wynne RH, Oliphant AJ (2015b) Reconstructing disturbance history for an intensively mined region by time-series analysis of Landsat imagery. Environmental Monitoring and Assessment 187:557

Li J, Zipper CE, Li S (2015c) Trajectory analysis of land disturbance and reclamation in surface coal-mine area by time-series NDVI. Transactions of the Chinese Society of Agricultural Engineering (in press)

Liaw A, Wiener M (2002) Classification and Regression by randomForest. R News 2:18-22

Markham B, Barsi J, Kvaran G, Ong L, Kaita E, Biggar S, Czapla-Myers J, Mishra N, Helder D (2014) Landsat-8 Operational Land Imager radiometric calibration and stability. Remote Sensing 6:12275-12308

Markham BL, Storey JC, Williams DL, Irons JR (2004) Landsat sensor performance: history and current status. Geoscience and Remote Sensing, IEEE Transactions on 42:2691-2694

McElfish JM, Beier AE (1990) Environmental Regulation of Coal Mining: SMCRA's Second Decade. Natural Resources Journal 31:707-712

Milici RC, Flores RM, Stricker GD (2013) Coal resources, reserves and peak coal production in the United States. International Journal of Coal Geology 113:109-115

Miller JH, Lemke D, Coulston J. (2013) The invasion of Southern forests by nonnative plants: Current and future occupation, with impacts, management strategies, and mitigation approaches. In The Southern forest futures project: Technical report. USDA Forest Service, General Technical Report SRS-178, Southern Research Station, Asheville, NC pp 397–456

Miller JH, Manning ST, Enloe SF (2010) A management guide for invasive plants in southern forests. USDA Forest Service, General Technical Report SRS-131, Southern Research Station, Asheville, NC pp 120

Natural Resource Conservation Service (2015) The PLANTS Database. U.S Department of Agriculture, National Plant Data Team. http://plants.usda.gov/java. Accessed 4/12/2015

NOAA (2015) 1981-2010 Normals for Big Stone Gap VA, US. U.S. National Oceanic and Atmospheric Administration. National Climate Data Center. http://www.ncdc.noaa.gov/cdo-web/datatools/normals. Accessed 7/21/2015

Nobis M, Hunziker U (2005) Automatic thresholding for hemispherical canopy-photographs based on edge detection. Agricultural and Forest Meteorology 128:243-250

Oliphant AJ, Li J, Wynne RH, Donovan PF, Zipper CE (2014) Identifying woody vegetation on coal surface mines using phenological indicators with multitemporal Landsat imagery. ISPRS-International Archives of the Photogrammetry, Remote Sensing and Spatial Information Sciences 1:339-345

Parsons S, Spader WE (1901) How to plan the home grounds. Doubleday, New York, NY

Peterson EB (2005) Estimating cover of an invasive grass (Bromus tectorum) using tobit regression and phenology derived from two dates of Landsat ETM+ data. International Journal of Remote Sensing 26:2491-2507

Prasad AM, Iverson LR, Liaw A (2006) Newer classification and regression tree techniques: bagging and random forests for ecological prediction. Ecosystems 9:181-199

Pyšek P, Richardson DM (2008) Traits associated with invasiveness in alien plants: where do we stand? In: Nentwig W (ed) Biological Invasions. Springer, Heidelberg, Germany, pp 97-125

Qi J, Chehbouni Al, Huete AR, Kerr YH, Sorooshian S (1994) A modified soil adjusted vegetation index. Remote Sensing of Environment 48:119-126

R-Core-Team (2014) R: A language and environment for statistical computing. R Foundation for Statistical Computing. http://www.R-project.org. Accessed 05/21/2015

Resasco J, Hale AN, Henry MC, Gorchov DL (2007) Detecting an invasive shrub in a deciduous forest understory using late-fall Landsat sensor imagery. International Journal of Remote Sensing 28:3739-3745

Rich PM (1990) Characterizing plant canopies with hemispherical photographs. Remote Sensing Reviews 5:13-29

Ridler TW, Calvard S (1978) Picture thresholding using an iterative selection method. IEEE transactions on Systems, Man and Cybernetics 8:630-632

Rodriguez-Galiano V, Ghimire B, Rogan J, Chica-Olmo M, Rigol-Sanchez J (2012) An assessment of the effectiveness of a random forest classifier for land-cover classification. ISPRS Journal of Photogrammetry and Remote Sensing 67:93-104

Rouse Jr J (1973) Monitoring the vernal advancement and retrogradation (green wave effect) of natural vegetation. Remote Sensing Center. Texas A&M Univ., College Station, TX

Roy David P, Wulder, MA, Loveland TR, Woodcock CE, Allen RG,Anderson MC, Helder D, Irons JR, Johnson DM, Kennedy R, Scambos TA, Schaaf CB, Schott JR, Shengm Y, Vermote EF, Belward, Bindschadler R, Cohen WB, Gao F, Hipple JD, Hostert P, Huntington J, Justice CO, Kilic A, Kovalskyy V, Lee ZP, Lymburner L, Masek JG, McCorkel J, Shuai Y, Trezza R, Vogelmann J, Wynne RH, Zhu Z (2014) Landsat-8: Science and product vision for terrestrial global change research. Remote Sensing of Environment 145:154-172

Schleppi P, Conedera M, Sedivy I, Thimonier A (2007) Correcting non-linearity and slope effects in the estimation of the leaf area index of forests from hemispherical photographs. Agricultural and Forest Meteorology 144:236-242

Seaber PR, Brahana J, Hollyday E (1988) Region 20, Appalachian Plateaus and Valley and Ridge. In: Bally AW, Palmer AR (eds) The Geology of North America: Hydrogeology, vol 0-2. Geological Society of America, pp 189-200

Sesnie SE, Gessler PE, Finegan B, Thessler S (2008) Integrating Landsat TM and SRTM-DEM derived variables with decision trees for habitat classification and change detection in complex neotropical environments. Remote Sensing of Environment 112:2145-2159

Sinclair J (1969) Reclamation after Surface Mining. In: Quarrying Opencast and Alluvial Mining. Springer, pp 318-327

Smith HG, Morse HH, Bernath GE, Gillogly LE, Briggs WM (1964) Classification and revegetating of strip-mine spoil banks. Ohio Journal of Science 64:168-175

Thimonier A, Sedivy I, Schleppi P (2010) Estimating leaf area index in different types of mature forest stands in Switzerland: a comparison of methods. European Journal of Forest Research 129:543-562

Tucker CJ (1979) Red and photographic infrared linear combinations for monitoring vegetation. Remote Sensing of Environment 8:127-150

Turner DP, Ritts WD, Cohen WB, Gower ST, Running SW, Zhao M, Costa MH, Kirschbaum AA, Ham JM, Saleska SR, Ahl DH (2006) Evaluation of MODIS NPP and GPP products across multiple biomes. Remote Sensing of Environment 102:282-292

US GAO (2009) Surface Coal Mining Characteristics of Mining in Mountainous Areas of Kentucky and West Virginia. United States Government Accountability Office. GAO-10-21 Washington, DC

U.S. Geologic Survey (2015a) Product Guide for Provisional Landsat 8 Surface Reflectance Product Version 1.5. U.S. Geological Survey, EROS Data Center. http://landsat.usgs.gov/documents/provisional_l8sr_product_guide.pdf. Accessed 7/21/2015

U.S. Geologic Survey (2015b) Product Guide: Landsat Surface Reflectance-Derived Spectral Indices Version 2.7. U.S. Geological Survey, EROS Data Center. http://landsat.usgs.gov/documents/si_product_guide.pdf. Accessed 7/21/2015

Wagner S (1998) Calibration of grey values of hemispherical photographs for image analysis. Agricultural and Forest Meteorology 90:103-117

Wilfong BN, Gorchov DL, Henry MC (2009) Detecting an invasive shrub in deciduous forest understories using remote sensing. Weed Science 57:512-520

Wilson EH, Sader SA (2002) Detection of forest harvest type using multiple dates of Landsat TM imagery. Remote Sensing of Environment 80:385-396

Wolkovich EM, Cleland EE (2010) The phenology of plant invasions: a community ecology perspective. Frontiers in Ecology and the Environment 9:287-294

Wolter PT, Mladenoff DJ, Host GE, Crow TR (1995) Improved forest classification in the Northern Lake States using multi-temporal Landsat imagery. Photogrammetric Engineering and Remote Sensing 61:1129-1144

Wulder MA, Masek JG, Cohen WB, Loveland TR, Woodcock CE (2012) Opening the archive: How free data has enabled the science and monitoring promise of Landsat. Remote Sensing of Environment 122:2-10

Yearsley EF, Samuel DE (1980) Use of reclaimed surface mines by foxes in West Virginia. The Journal of Wildlife Management 44:729-734

Zipper C, Burger J, McGrath J, Rodrigue J, Holtzman G (2011a) Forest restoration potentials of coal-mined lands in the eastern United States. Journal of Environmental Quality 40:1567-1577

Zipper C, Burger J, Skousen J, Angel P, Barton C, Davis V, Franklin J (2011b) Restoring Forests and Associated Ecosystem Services on Appalachian Coal Surface Mines. Environmental Management 47:751-765

APPENDIX A

Supporting Reference Data Collection

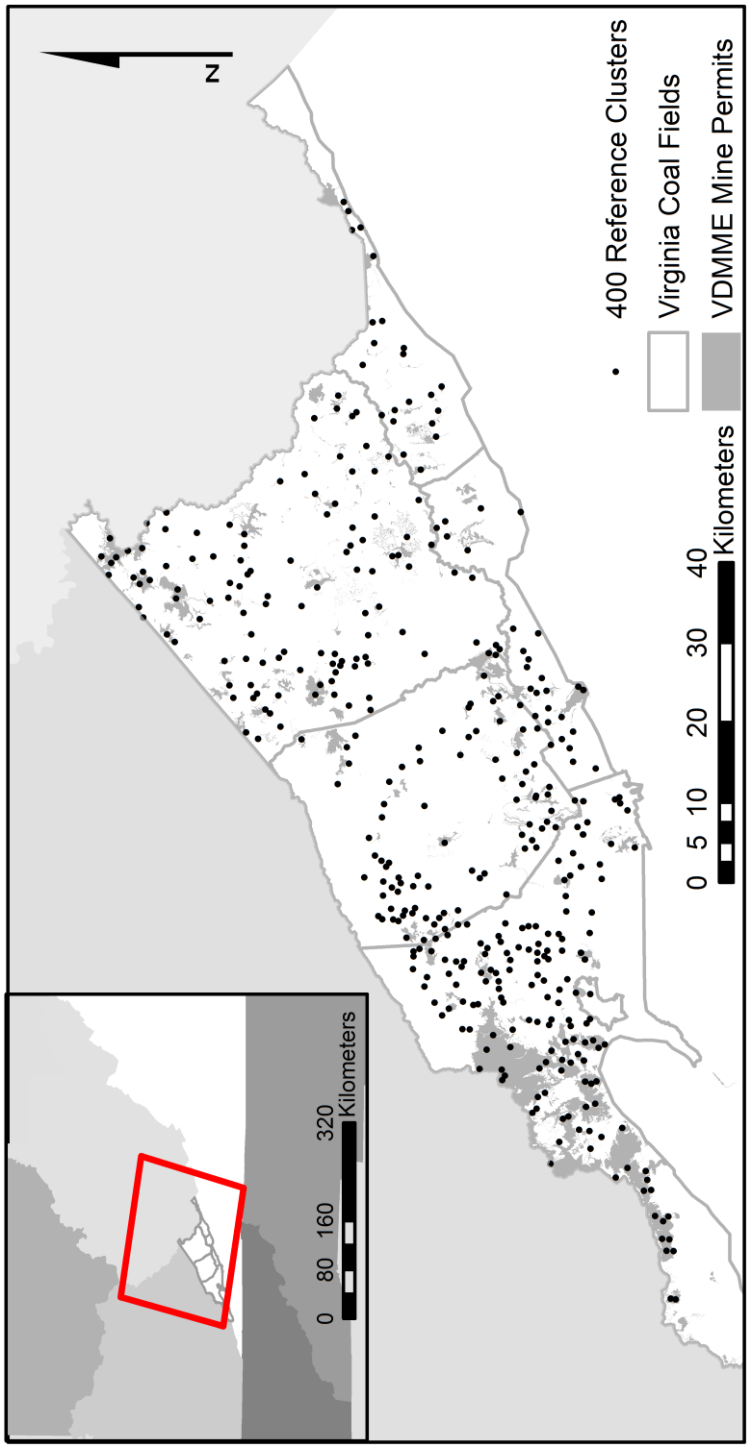

Figure A.1 Location of 400 reference clusters over VDMME mine permits. Clusters were on Buchannan, Dickenson, Lee, Russel, Scott, Tazewell, Wise Counties in Virginia. The red box on the insert map shows the footprint of Landsat scene path 18 row 34.

Table A.1 Sample reference data acquired from classification of 400 clusters. The X and Y coordinates are in UTM 17 N and the datum is WGS 1984. AO= autumn olive.

Pixel #	Xcoord	Ycoord	Class	Pixel #	Xcoord	Ycoord	Class
1	325740	4080630	AO	50	347880	4092030	AO
2	325770	4080630	AO	51	347910	4092030	AO
3	325800	4080630	AO	52	363240	4093110	AO
4	325710	4080750	AO	53	363270	4093110	AO
5	325740	4080750	AO	54	363210	4093170	AO
6	325770	4080750	AO	55	363240	4093170	AO
7	325800	4080750	AO	56	363270	4093170	AO
8	325830	4080750	AO	57	363300	4093170	AO
9	325830	4080780	AO	58	363240	4093200	AO
10	328680	4081500	AO	59	363270	4093200	AO
11	328650	4081560	AO	60	363300	4093200	AO
12	328650	4081620	AO	61	363240	4093230	AO
13	328680	4081620	AO	62	363270	4093230	AO
14	339630	4085610	AO	63	363300	4093230	AO
15	339660	4085610	AO	64	363330	4093230	AO
16	339630	4085640	AO	65	363360	4093230	AO
17	339570	4085670	AO	66	396000	4095630	AO
18	339600	4085670	AO	67	396000	4095660	AO
19	376350	4090470	AO	68	396030	4095660	AO
20	376410	4090500	AO	69	396000	4095690	AO
21	376440	4090500	AO	70	396030	4095690	AO
22	376440	4090530	AO	71	395970	4095720	AO
23	356370	4089720	AO	72	396000	4095720	AO
24	356430	4089750	AO	73	343500	4096080	AO
25	356430	4089780	AO	74	343530	4096080	AO
26	353310	4089660	AO	75	343560	4096080	AO
27	353370	4089660	AO	76	343470	4096110	AO
28	353310	4089690	AO	77	343500	4096110	AO
29	353400	4089690	AO	78	343440	4096140	AO
30	353250	4089780	AO	79	398310	4097340	AO
31	345300	4089510	AO	80	398310	4097370	AO
32	345300	4089540	AO	81	398280	4097400	AO
33	345270	4089600	AO	82	398310	4097400	AO
34	345300	4089600	AO	83	398310	4097430	AO
35	345270	4089630	AO	84	399300	4098000	AO
36	345450	4090200	AO	85	399270	4098030	AO
37	345420	4090230	AO	86	399300	4098030	AO
38	345450	4090230	AO	87	399240	4098060	AO

APPENDIX B

Hemispherical Results

April 12 2014

May 5th 2014

Figure B.1 Hemispherical photos showing difference between autumn olive and hardwood phenology. Images were acquired during the 2014 growing season on the field study site in Christiansburg, Virginia.

Table B.1 Leaf area index calculated from hemispherical photos showing difference between autumn olive and hardwood phenology during the 2014 growing season on the field study site in Christiansburg, Virginia.

DOY	Date	Autumn olive LAI	Forest LAI
88	3/29	0.96	0.65
95	4/05	1.12	0.54
102	4/12	1.40	0.53
123	5/03	2.06	1.05
131	5/11	2.47	2.82
153			3.71
170	6/19	2.97	4.32
182	7/01	3.08	
197	7/16	3.48	3.54
216	8/04	3.31	3.69
228	8/16	3.10	4.00
242	8/30	2.72	3.34
257	9/14	2.77	3.25
271	9/28	2.54	3.07
278	10/05	2.29	
292	10/19	2.00	1.87
305	11/01	1.55	0.91

APPENDIX C

Supporting Documentation for randomForest Model

```
Call:
 randomForest(x = sdata@data[, 5:ncol(sdata@data)], y = as.factor(sdata@data[,
"BinaryT"]), ntree = 501, mtry = 20, importance = TRUE)
               Type of random forest: classification
                     Number of trees: 501    No. of variables tried at each split: 20
                      OOB estimate of error rate: 1.58%

Confusion matrix:
       Aos  Oth class.error
Aos 374      0  0.00000000
Oth  22    998  0.02156863

# Load raster
aster <-readGDAL('ENVIimage')
rasterStack <- stack(raster)
extent(rasterStack)

# Load training data
trainingFile <- readOGR(dsn=dir, layer="ShapefileName")
trainingFile[,1]
trainingData <- as.data.frame(extract(rasterStack, trainingFile))trainingFile@data =
                  data.frame(trainingFile@data, trainingData[match(rownames(trainingFile@data),
                  rownames(trainingData)),])

# Run randomForest
RFmodel <- randomForest(x=trainingFile@data[,5:ncol(trainingFile@data)],
                 y=as.factor(trainingFile@data[,"Binary"]), ntree=501, mtry=20, importance=TRUE)

print(RFmodel)
OOB estimate of error rate: 1.58%
Confusion matrix:
       Aos  Oth class.error
Aos 374      0  0.00000000
Oth  22    998  0.02156863

# Plot error convergence
plot(RFmodel)

# Variable of importance
varImportance <- importance(RFmodel)
varUsed <- varUsed(RFmodel)
write.csv(varImportance, "varImportance.csv", overwrite=FALSE)

# Generate RF classified Image
RFimage <- predict(rasterStack, RFmodel, filename='RFmodel.tif', type="response",
                index=1, na.rm=TRUE, progress="window", overwrite=FALSE)
```

Figure C.1 Scripts used to call ramdomForest classifier

Table C.1 The randomForest variable of importance table. AO = autumn olive

Scene & Band	% AO Accuracy Decrease	% NotAO Accuracy Decrease	Mean % Accuracy Decrease	Overall Variable of Importance
116_b5	24.1	19.1	27.3	1
55_nbr2	22.5	12.9	22.8	2
116_b3	18.5	6.8	19.6	3
116_nbr2	14.9	8.5	15.5	5
74_nbr2	14.4	8.0	14.9	7
90_nbr2	14.3	9.5	14.3	9
263_b5	14.0	5.6	13.0	13
116_b6	14.0	7.8	15.2	6
116_msavi	13.8	12.3	16.1	4
260_b5	13.8	4.2	13.0	14
116_evi	12.6	10.9	14.3	10
263_nbr2	12.2	5.3	13.0	12
10_b5	12.1	11.1	14.6	8
260_nbr2	12.0	5.2	12.6	16
260_evi	11.9	4.8	12.8	15
95_ndmi	11.7	8.3	12.4	17
260_msavi	11.4	2.0	12.4	18
116_savi	11.4	10.8	13.7	11
10_b4	11.3	5.7	11.2	26
260_ndvi	11.1	5.8	11.9	20
260_b6	11.0	5.7	10.7	36
260_b4	10.9	6.1	11.3	24
260_b3	10.5	5.4	11.5	23
116_b2	10.4	5.3	11.9	21
90_ndmi	10.3	6.3	11.0	30
95_nbr2	10.1	4.7	8.9	64
116_b7	10.0	7.3	10.8	34
90_b6	10.0	7.6	10.6	38
260_b7	9.9	5.6	10.2	45
260_savi	9.9	5.4	11.8	22
10_b3	9.8	8.4	11.3	25
55_ndvi	9.7	6.9	10.9	32
116_b1	9.7	5.1	10.8	33
55_nbr	9.7	6.8	10.0	47
74_ndvi	9.6	6.7	11.1	28
95_savi	9.5	5.3	7.8	92
260_b1	9.4	4.3	10.2	44
55_ndmi	9.4	4.8	9.1	59
10_b1	9.3	9.6	12.2	19
263_evi	9.2	3.0	8.6	74

95_evi	9.2	4.5	8.4	77
263_b2	9.1	6.6	10.2	46
263_ndmi	9.1	3.9	8.7	71
260_b2	9.1	4.4	10.7	37
90_ndvi	9.0	4.6	8.4	78
95_nbr	9.0	5.8	11.0	29
10_nbr2	9.0	5.3	9.5	53
263_ndvi	8.9	6.0	9.1	60
10_ndmi	8.9	4.1	8.2	83
263_nbr	8.8	2.6	8.7	73
263_b4	8.8	7.6	10.5	40
90_nbr	8.8	5.5	10.4	41
90_b3	8.8	6.3	9.6	50
95_ndvi	8.8	4.3	9.0	62
260_nbr	8.7	4.7	9.9	48
263_msavi	8.7	3.5	8.9	66
55_evi	8.6	6.5	10.3	43
263_b3	8.6	7.9	10.4	42
263_savi	8.6	3.1	8.3	81
116_nbr	8.5	4.5	8.8	67
10_b2	8.5	8.6	11.1	27
95_b6	8.4	4.7	8.3	80
10_ndvi	8.4	7.6	10.9	31
90_b5	8.3	7.8	10.8	35
90_b1	8.3	6.1	9.4	54
116_ndvi	8.2	5.7	10.5	39
263_b6	8.2	4.8	8.8	68
116_b4	8.0	5.8	9.0	61
10_evi	8.0	5.0	9.5	51
10_b6	8.0	4.4	9.0	63
90_b2	7.8	4.5	7.8	94
90_savi	7.7	3.9	8.2	82
10_savi	7.7	5.1	9.3	55
74_b1	7.6	4.5	9.3	56
10_b7	7.6	6.2	9.7	49
263_b7	7.5	5.1	8.3	79
260_ndmi	7.5	4.2	8.5	76
74_b2	7.4	3.4	8.8	69
95_msavi	7.4	5.3	7.2	104
95_b5	7.4	4.9	7.3	102
95_b1	7.4	5.3	8.7	72
10_nbr	7.3	5.0	8.0	88
90_msavi	7.2	5.5	7.5	97
55_b1	7.2	4.7	7.9	89
263_b1	7.1	7.3	9.5	52

10_msavi	7.1	5.1	9.2	57
90_evi	7.0	4.3	7.6	95
95_b7	6.8	3.5	8.1	87
74_b5	6.7	5.2	7.4	101
55_savi	6.7	6.0	9.2	58
74_b4	6.6	1.8	7.3	103
74_ndmi	6.6	5.3	7.8	93
95_b4	6.6	3.2	7.5	98
116_ndmi	6.5	5.6	8.9	65
74_savi	6.4	5.7	8.7	70
55_b7	6.4	6.4	8.5	75
74_b7	6.4	2.5	7.0	107
74_msavi	6.4	5.6	8.1	86
95_b2	6.4	5.3	7.1	105
55_msavi	6.3	5.0	8.2	84
55_b5	6.3	5.1	8.1	85
55_b3	6.3	3.6	7.4	100
55_b6	6.3	3.6	7.5	96
90_b7	6.3	3.4	6.5	108
90_b4	6.1	4.0	6.1	111
74_nbr	6.1	5.6	7.9	91
74_evi	6.0	4.4	7.5	99
74_b6	6.0	2.9	6.3	110
95_b3	6.0	4.4	7.9	90
74_b3	5.9	3.5	7.0	106
55_b2	5.5	4.1	6.4	109
55_b4	4.9	3.4	5.9	112

APPENDIX D

Autumn Olive on Mined Lands

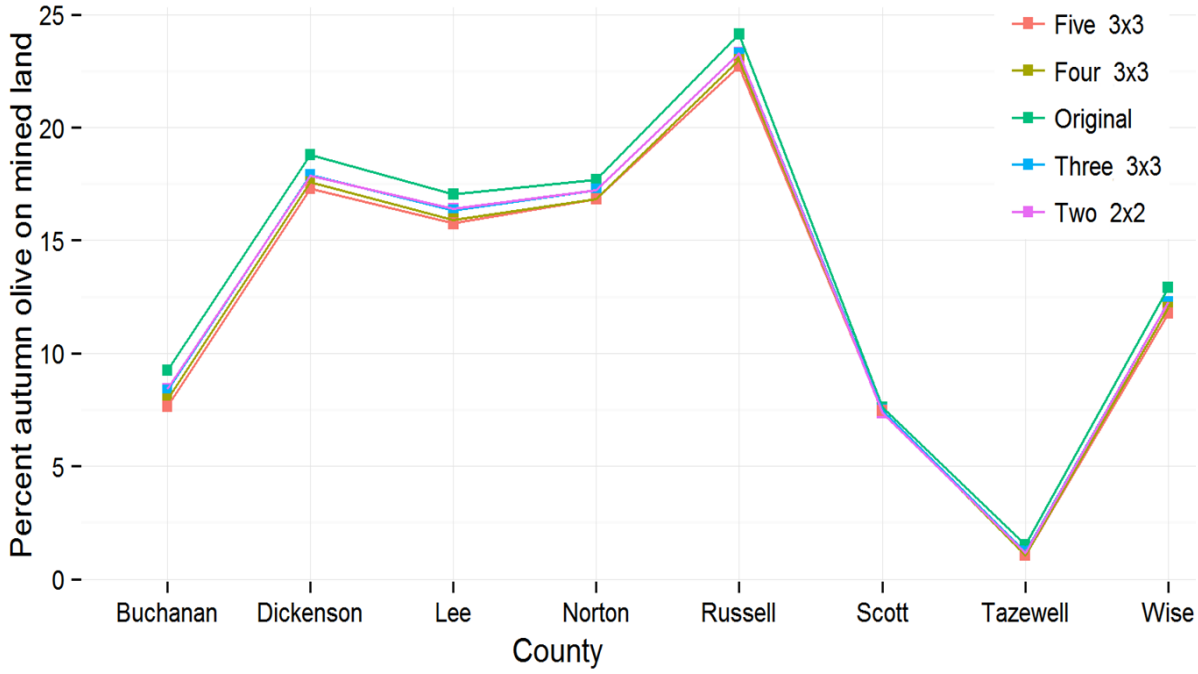

Figure D.1 Percent of autumn olive in the coal mining region for each county plotted for each focal filter examined as of 2014.

Table D.1 Total area and area of autumn olive by year of first disturbance.

Class	Total Area (ha)	Area of Autumn Olive (ha)	Percent Autumn Olive Cover
Non-mined land	928312.11	30850.2	3.32
Persistent Vegetation	336162.42	3749.4	1.12
Mining detected in 1984	7137.27	1038.6	14.55
Mining detected in 1985	1248.93	189.99	15.21
Mining detected in 1986	947.88	141.03	14.88
Mining detected in 1987	842.04	137.43	16.32
Mining detected in 1988	1098.9	170.55	15.52
Mining detected in 1989	605.16	81.99	13.55
Mining detected in 1990	813.69	155.07	19.06
Mining detected in 1992	1007.64	183.33	18.19
Mining detected in 1993	458.64	118.35	25.80
Mining detected in 1994	1334.61	274.86	20.59
Mining detected in 1995	812.07	150.84	18.57
Mining detected in 1997	1704.42	324	19.01
Mining detected in 1998	761.4	157.41	20.67
Mining detected in 1999	980.82	195.21	19.90
Mining detected in 2000	611.37	88.47	14.47
Mining detected in 2001	1184.13	197.73	16.70
Mining detected in 2002	820.8	71.37	8.70
Mining detected in 2003	955.26	63.63	6.66
Mining detected in 2004	1071.45	36.72	3.43
Mining detected in 2005	964.89	15.39	1.60
Mining detected in 2007	2126.88	26.82	1.26
Mining detected in 2008	922.95	2.16	0.23
Mining detected in 2010	1190.7	1.8	0.15
Mining detected in 2011	682.92	0.63	0.09
Disturbance outside mining permits	28272.06	1446.84	5.12
Open Water	686.25	1.62	0.24
Disturbance inside mining permits	6588.9	902.61	13.70

Table D.2 Percent coverage of autumn olive per year of disturbance per county.

Class	Buchanan County	Dickenson County	Lee County	Russell County	Tazewell County	Wise County
Nom-mined land	4.6	0	0.6	2.1	4.7	3.4
Persistent vegetation	0.5	1.7	1.1	1.3	0.3	2.3
Mining detected in 1984	10.4	19.2	10.5	6.5	3.2	15.8
Mining detected in 1985	8.0	23.4	10.0	18.5	2.2	14.9
Mining detected in 1986	7.3	16.0	15.7	12.8	0.5	17.3
Mining detected in 1987	13.0	13.3	16.0	4.2	0	18.3
Mining detected in 1988	13.0	13.0	10.4	11.7	0	17.3
Mining detected in 1989	7.7	12.3	0.3	8.8	4.2	16.0
Mining detected in 1990	16.0	25.0	10.7	12.8	0.1	22.2
Mining detected in 1992	6.4	21.3	13.9	40.1	2.7	19.2
Mining detected in 1993	10.5	36.7	22.0	40.9	7.3	20.5
Mining detected in 1994	14.3	25.5	38.8	24.9	0.6	16.4
Mining detected in 1995	10.9	12.0	35.1	43.2	13.1	14.9
Mining detected in 1997	14.2	26.0	39.3	19.4	0	14.5
Mining detected in 1998	9.9	32.0	26.2	60.1	0	13.2
Mining detected in 1999	16.3	28.8	16.4	41.8	0	13.9
Mining detected in 2000	14.4	25.8	8.7	28.4	0	10.7
Mining detected in 2001	14.0	20.3	11.1	43.9	0	12.5
Mining detected in 2002	7.2	5.7	16.5	40.2	0	7.1
Mining detected in 2003	0.9	20.2	4.4	27.8	0	4.6
Mining detected in 2004	3.4	0.6	9.9	4.1	0	3.5
Mining detected in 2005	1.5	1.3	1.3	1.1	1.0	1.8
Mining detected in 2007	2.3	0.8	1.2	0.5	0	0.9
Mining detected in 2008	0	0.7	0	0.7	0	0.3
Mining detected in 2010	0.3	0.3	0	0	0	0.1
Mining detected in 2011	0	0	0	0	0	0.2
Open Water	3.1	0	0	2.4	2.6	0.2
Disturbance inside the mining permits	7.2	18.8	8.7	13.8	2.7	15.3
Disturbance outside mining permits	2.2	8.1	5.0	5.9	2.6	5.7